

1

2 **Interactions of SARS-CoV-2 envelope protein with amilorides correlate with**
3 **antiviral activity**

4 Sang Ho Park¹, Haley Siddiqi¹, Daniela V. Castro¹, Anna De Angelis¹, Aaron L. Oom², Charlotte A.
5 Stoneham³, Mary K. Lewinski³, Alex E. Clark^{3,4}, Ben A. Croker⁵, Aaron F. Carlin³, John Guatelli³, and
6 Stanley J. Opella^{1*}

7 ¹Department of Chemistry and Biochemistry, University of California San Diego, La Jolla, CA 92093,
8 USA

9 ²Department of Medicine, University of California San Diego, La Jolla, CA 92093, USA.

10 ³Division of Infectious Diseases and Global Public Health, Department of Medicine; University of
11 California San Diego School of Medicine, 9500 Gilman Drive, La Jolla, CA 92093, USA.

12 ⁴Department of Cellular and Molecular Medicine, University of California San Diego, La Jolla, CA
13 92093, USA.

14 ⁵Department of Pediatrics, University of California San Diego, La Jolla, CA, USA

15

16 Short title: Interactions of SARS-CoV-2 E with amilorides correlate with antiviral activity

17

18 *Corresponding author E-mail address: sopella@ucsd.edu

19 **Abstract**

20 SARS-CoV-2 is the novel coronavirus that is the causative agent of COVID-19, a sometimes-lethal
21 respiratory infection responsible for a world-wide pandemic. The envelope (E) protein, one of four
22 structural proteins encoded in the viral genome, is a 75-residue integral membrane protein whose
23 transmembrane domain exhibits ion channel activity and whose cytoplasmic domain participates in
24 protein-protein interactions. These activities contribute to several aspects of the viral replication-cycle,
25 including virion assembly, budding, release, and pathogenesis. Here, we describe the structure and
26 dynamics of full-length SARS-CoV-2 E protein in hexadecylphosphocholine micelles by NMR
27 spectroscopy. We also characterized its interactions with four putative ion channel inhibitors. The
28 chemical shift index and dipolar wave plots establish that E protein consists of a long transmembrane
29 helix (residues 8-43) and a short cytoplasmic helix (residues 53-60) connected by a complex linker that
30 exhibits some internal mobility. The conformations of the N-terminal transmembrane domain and the C-
31 terminal cytoplasmic domain are unaffected by truncation from the intact protein. The chemical shift
32 perturbations of E protein spectra induced by the addition of the inhibitors demonstrate that the N-
33 terminal region (residues 6-18) is the principal binding site. The binding affinity of the inhibitors to E
34 protein in micelles correlates with their antiviral potency in Vero E6 cells: HMA \approx EIPA > DMA >>
35 Amiloride, suggesting that bulky hydrophobic groups in the 5' position of the amiloride pyrazine ring
36 play essential roles in binding to E protein and in antiviral activity. An N15A mutation increased the
37 production of virus-like particles, induced significant chemical shift changes from residues in the
38 inhibitor binding site, and abolished HMA binding, suggesting that Asn15 plays a key role in maintaining
39 the protein conformation near the binding site. These studies provide the foundation for complete
40 structure determination of E protein and for structure-based drug discovery targeting this protein.

41 **Author Summary**

42 The novel coronavirus SARS-CoV-2, the causative agent of the world-wide pandemic of COVID-19,
43 has become one of the greatest threats to human health. While rapid progress has been made in the
44 development of vaccines, drug discovery has lagged, partly due to the lack of atomic-resolution
45 structures of the free and drug-bound forms of the viral proteins. The SARS-CoV-2 envelope (E)
46 protein, with its multiple activities that contribute to viral replication, is widely regarded as a potential
47 target for COVID-19 treatment. As structural information is essential for drug discovery, we established
48 an efficient sample preparation system for biochemical and structural studies of intact full-length SARS-
49 CoV-2 E protein and characterized its structure and dynamics. We also characterized the interactions
50 of amilorides with specific E protein residues and correlated this with their antiviral activity during viral
51 replication. The binding affinity of the amilorides to E protein correlated with their antiviral potency,
52 suggesting that E protein is indeed the likely target of their antiviral activity. We found that residue
53 asparagine15 plays an important role in maintaining the conformation of the amiloride binding site,
54 providing molecular guidance for the design of inhibitors targeting E protein.

55

56 **Introduction**

57 Severe acute respiratory syndrome coronavirus 2 (SARS-CoV-2) has garnered attention as the
58 causative agent of the disease COVID-19. It is an enveloped RNA virus classified as a beta coronavirus
59 [1] similar to the previously studied SARS-CoV [2] and MERS-CoV [3] viruses. While rapid progress
60 has been made in analyzing the SARS-CoV-2 genome [4] and the development of protective vaccines
61 [5, 6], the discovery of therapeutics has lagged, largely due to the lack of structures of the viral proteins
62 and information about their specific roles in infection, replication, and propagation. Here we apply NMR
63 spectroscopy to the envelope (E) protein, one of the structural membrane proteins of SARS-CoV-2, in
64 order to characterize its secondary structure, drug binding site, and effects of selected single-site
65 mutations on its structure and binding of amiloride compounds. To accomplish these goals, the results
66 from NMR on E protein are augmented by those from virological experiments on infected cells [7] as
67 well as the measurement of antiviral activities of amiloride compounds.

68 The approximately 30kb RNA genome of SARS-CoV-2 encodes for 29 proteins
69 (www.ncbi.nlm.nih.gov/nuccore/NC_045512). The most abundant are four structural proteins,
70 membrane (M), envelope (E), nucleocapsid (N), and spike (S), of which M, E, and S are integral
71 membrane proteins embedded in the lipid bilayer of the viral envelope (Fig1). Each of these proteins
72 exists as a homo-oligomer under some experimental conditions: a dimer or dimer of dimers for M [8], a
73 pentamer for E [9, 10], and a trimer for S [11]. The biological relevance of E protein comes from its
74 involvement in key aspects of the virus lifecycle, including infection, replication, assembly, budding, and
75 pathogenesis [12]. Furthermore, recombinant coronaviruses lacking E protein exhibit significantly
76 reduced viral titers, crippled viral maturation, and yield propagation incompetent progeny [13-15].
77 SARS-CoV-2 E protein is a hydrophobic 75-residue protein with an amino acid sequence nearly
78 identical to that of SARS-CoV E protein (S1 Fig) [12]. Since E protein is a viral membrane-spanning
79 miniprotein [16], a recurring question is whether it is a viroporin. Although ion-channel activity has been
80 detected in a variety of preparations it lacks sequence homology with any of the well-established

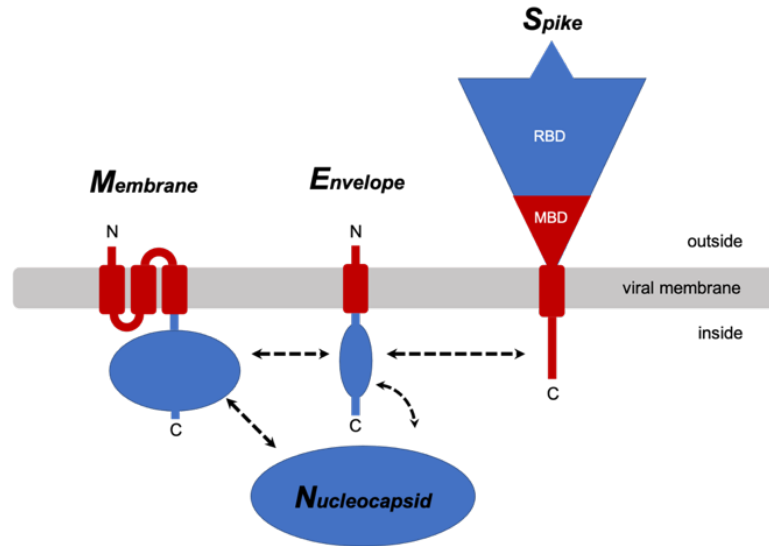
81 viroporins, and there is a notable absence of charged sidechains on the interior of a pore formed by
82 pentamers of the protein in membrane environments [9, 10, 17, 18].

83 The importance of E protein for viral replication and maturation is well established, making it an
84 attractive target for antiviral drugs. Drug design requires high-resolution structures of the protein
85 receptor in its bound and free states. Small membrane proteins are notoriously difficult to crystallize in
86 their native states in liquid crystalline membrane bilayers for X-ray crystallography and are too small for
87 cryoEM to be effective. While generally suited for NMR spectroscopy, careful consideration of the
88 membrane-like environment of the samples and the NMR experimental methods are essential [19].
89 Even the earliest NMR studies of membrane proteins showed that caution is called for when using
90 micelle environments [20], because of the potential for aggregation and structural distortions [21, 22].
91 Nonetheless, careful optimization of sample conditions has enabled solution NMR to provide valid
92 structural information about membrane proteins that could be obtained in no other way. Moreover, we
93 have found it essential to prepare samples of membrane proteins in micelles that yield high-resolution
94 solution NMR spectra in order to verify that they integrate into an amphipathic membrane-like
95 environment, are chemically pure, not mis-folded, and not aggregated before initiating significantly
96 more demanding solid-state NMR studies of phospholipid bilayer samples. In order to ensure that solid-
97 state NMR experiments are performed under near-native conditions, both the protein and the bilayers
98 must be fully characterized to ensure that the protein is in its biologically active conformation and stably
99 embedded in liquid crystalline, fully hydrated phospholipid bilayers at high lipid to protein ratios.

100 Here we describe solution NMR studies of full-length SARS-CoV-2 E protein and several truncated
101 and mutated constructs in highly optimized n-hexadecylphosphocholine (HPC; fos-choline-16) micelles.
102 Because our novel purification scheme starts by using HPC to solubilize the protein-containing
103 inclusion bodies and HPC is present during all subsequent steps, the polypeptides are never exposed
104 to any other detergent or lipid, which would require exchanges, or to any organic solvent, which would
105 require refolding. The success of the HPC-based protein purification and sample preparation scheme

106 results in the well-resolved solution NMR spectra presented in the Figures. Furthermore, this scheme
107 leads directly to the preparation of magnetically aligned bilayer samples that are well-suited for protein
108 structure determination by oriented sample (OS) solid-state NMR [23].

109 Previous structural studies of coronavirus E protein, especially by NMR, have been simplified by
110 using relatively short polypeptides with sequences corresponding to a substantial portion of the N-
111 terminal domain containing the transmembrane helix that forms ion channels through homo-
112 oligomerization as well as residues responsible for drug binding [9, 10, 17, 18]. To date, no structural
113 data have been presented for any full-length coronavirus E protein. Structures of a 31-residue synthetic
114 polypeptide (residues 8-38) [17] and of a longer 58-residue expressed polypeptide (residues 8-65)
115 containing three Cys to Ala mutations and non-native 23-residues in its N-terminus [9, 18] have been
116 described for sequences from the SARS-CoV E protein. They are highly relevant to studies of the
117 SARS-CoV-2 E protein because the amino acid sequences of these two proteins are identical between
118 residues 1 and 68. The partial E protein structures determined for these polypeptides in micelles by
119 solution NMR have been modeled as pentamers [9, 17, 18]. In addition, an expressed 31-residue
120 polypeptide with the same sequence as residues 8-38 of SARS-CoV-2 E protein has been studied by
121 magic angle spinning (MAS) solid-state NMR in the presence of phospholipids, and its structure has
122 also been modeled as a pentamer [10]. There are significant differences between the conclusions
123 derived from these earlier studies of relatively small polypeptides missing the N-terminal seven
124 residues and those presented here based on studies of full-length protein (residues 1-75) and two
125 overlapping constructs encompassing the N-terminal domain (residues 1-39) and the C-terminal
126 domain (residues 36-75). Notably, the wild-type N-terminal 39-residues are present in both the full-
127 length and C-terminal truncated proteins.



128

129 **Fig 1. Cartoon representations of the four structural proteins of SARS-CoV-2.** The membrane-associated
130 portions of the membrane (M) protein, envelope (E) protein, and spike (S) protein are shown in red, and the extra-
131 and intra- cellular portions are shown in blue. Proposed intraviral protein-protein interactions are indicated by the
132 dashed arrows. RBD: receptor-binding domain; MBD: membrane-binding domain. Nucleocapsid (N) is the fourth
133 structural protein.

134 While the transmembrane helix of E protein is thought to be largely responsible for homo-
135 oligomerization and ion-channel activity [17, 18], its highly hydrophobic nature makes modeling a
136 channel similar to those of other miniproteins difficult [16]. Intraviral interactions between E and M
137 proteins have been shown to involve the C-terminal domains of both proteins [24, 25]. The triple
138 cysteine motif (C40, C43, and C44) in E protein has been proposed to associate with the cysteine-rich
139 C-terminal region of S protein by forming intermolecular disulfide bonds [26]. E protein also interacts
140 with host proteins [12]. The C-terminal four residues, DLLV, have been identified as a PDZ-binding
141 motif that interacts with the tight junction-associated PALS1 protein [27]. The C-terminal region of E
142 protein that resembles the bromodomain binding site of histone H3 interacts with bromodomains 2 and
143 4 via acetylated Lys63, which is involved in the regulation of gene transcription [28]. These studies
144 provide strong biological and mechanistic justification for considering coronavirus E protein as a
145 potential drug target. Extending structural studies to samples of the full-length protein that include the
146 complete drug binding site as well as the native N-terminus, C-terminus, and other features is essential

147 for structure-based drug discovery. Equally important is the correlation of structural features of the
148 protein with specific biological activities of the virus as it reproduces in human cells.

149 The channel activity of E protein has been suggested to play a role in viral replication [29]. A well-
150 characterized channel blocker, hexamethylene amiloride (HMA), inhibits ion channel conductance of E
151 proteins from HCoV-229E and MHV as well as virus replication in cultured cells [30]. HMA also inhibits
152 the channel conductance of transmembrane-containing synthetic and expressed polypeptides from the
153 SARS-CoV E protein [17, 18]. Although interactions of HMA with E protein of SARS-CoV have been
154 detected in prior studies, the residues in the HMA binding site identified by NMR chemical shift
155 perturbations varied quite a bit depending upon the specific E protein constructs and experimental
156 conditions [9, 10, 17, 18].

157 Here we characterize the secondary structure of full-length E protein from SARS-CoV-2 in HPC
158 micelles. We also map out the complete binding sites of amiloride and three amiloride derivatives
159 (dimethyl amiloride (DMA), ethyl isopropyl amiloride (EIPA), and HMA) and compare their binding
160 properties. Importantly, the antiviral potency of the amiloride derivatives against SARS-CoV-2 infection
161 of Vero E6 cells correlates well with their strength of binding as observed in the NMR experiments. The
162 N15A and V25F mutations of the SARS-CoV-2 E protein have very different effects on the NMR
163 spectra of the protein; the N15A mutation causes greater chemical shift perturbations over a larger
164 region of the protein than the V25F mutation, which causes only minor changes near the site of the
165 amino acid substitution. These mutations affect production of virus-like particle (VLP) and, in the case
166 of N15A, the binding of HMA.

167 **Results**

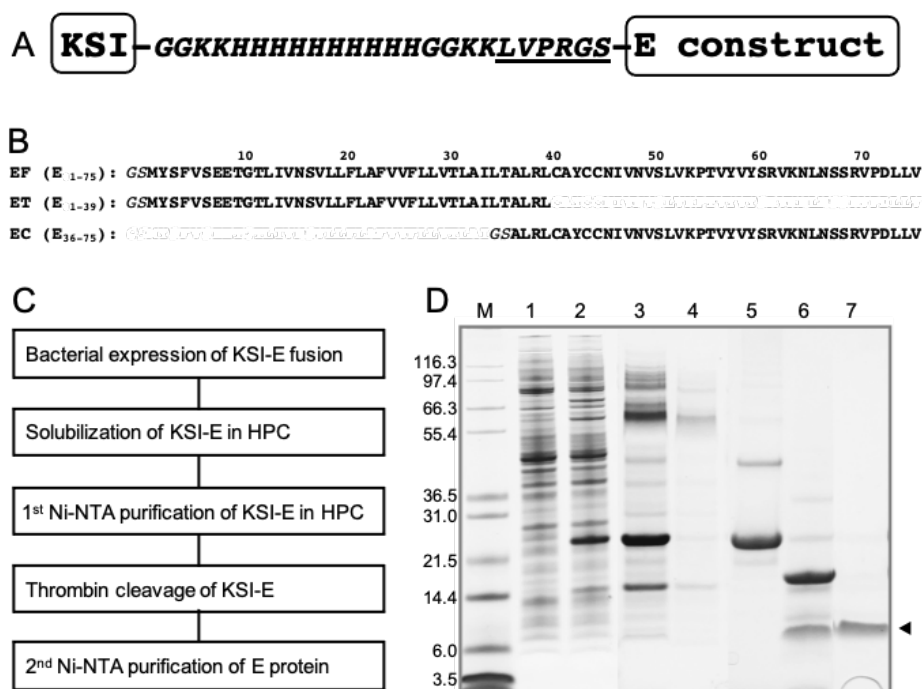
168 **Preparation of full-length SARS-CoV-2 E protein**

169 In order to apply NMR spectroscopy to full-length E protein of SARS-CoV-2 it was essential to develop
170 and implement an entirely new sample preparation scheme. We were unable to overcome the
171 difficulties inherent in dealing with hydrophobic membrane proteins in the case of E protein using
172 approaches that we had previously applied successfully to viral, bacterial, and human membrane
173 proteins with between one and seven transmembrane helices [31-36]. These preparative difficulties
174 may be among the reasons that prior NMR studies of E protein have been limited to N- and C- terminal
175 truncated constructs with only 31 or 58 residues, which are notably missing the seven N-terminal
176 residues that our data show to be essential components of the drug-binding site.

177 The ketosteroid isomerase (KSI) fusion partner facilitated the expression of high levels of three
178 different E protein constructs, including the full-length protein (residues 1-75), as inclusion bodies in *E.*
179 *coli* [32, 37]. A ten-residue His-tag followed by a six-residue thrombin cleavage site, LPVRGS, inserted
180 between the KSI and the E protein sequences enabled purification by Ni-affinity chromatography and
181 efficient enzymatic cleavage (Fig 2C). The resulting E protein sequence differs from that of the SARS-
182 CoV-2 isolate Wuhan-Hu-1 (NC_045512) only by the presence of two additional residues (GlySer) at
183 the N-terminus that were originally part of the thrombin cleavage site (Fig 2B).

184 Our scheme for the expression and purification of the full-length wild-type and mutated, and
185 truncated constructs of E protein is outlined in Fig 2C. They were all expressed in *E. coli* as fusion
186 proteins and sequestered in inclusion bodies (Fig 2D). After screening many detergents informed by
187 our extensive experience with solution NMR studies of membrane proteins [20, 31, 38-41] and
188 thorough literature reviews [22], we found that the highest resolution spectra were obtained when E
189 protein was solubilized in hexadecylphosphocholine (HPC, fos-choline-16) micelles. Chemically similar
190 to the commonly used dodecylphosphocholine (DPC) [42], HPC has been previously considered for,
191 but, to our knowledge, not used to study membrane proteins by NMR [43]. HPC is notable for its low
192 critical micelle concentration (CMC, 13 μ M) (www.anatrace.com). It is able to solubilize E protein and
193 other hydrophobic membrane proteins, is effective with Ni-affinity chromatography, and at a low

194 concentration of 0.05% w/v (1.23 mM) does not interfere with specific thrombin cleavage. This
 195 approach is highly efficient and, significantly, obviates the need for detergent exchanges or exposure to
 196 organic solvents at any stage of the isolation and purification process. Purified full-length E (EF) in HPC
 197 micelles runs as a monomer (~ 8.5 kDa) with a narrow band on SDS-PAGE (Fig 2D). By contrast, as
 198 observed by others [44], it runs as a broad ill-defined band on PFO (perfluorooctanoic acid)-PAGE that
 199 may demonstrate the presence of an oligomeric species (Fig 9D) generally assumed to be a pentamer
 200 consistent with its viroporin-like properties [9, 10, 17, 18, 44, 45]. All samples used in the NMR
 201 experiments were prepared directly from protein solubilized in HPC from start to finish. The resulting
 202 NMR spectra are well-resolved with narrow resonance linewidths. The samples exhibit excellent long-
 203 term stability at 50°C (Fig 3).



204

205 **Fig 2. Heterologous expression and purification of the full-length SARS-CoV-2 E protein and truncated**
 206 **protein constructs.** (A) Design of SARS-CoV-2 E protein and KSI fusion protein construct utilized for efficient
 207 bacterial expression and purification. The six residues (LVPRGS) that define the thrombin cleavage site are
 208 underlined. (B) Amino acid sequences of the polypeptides used here: full-length E protein (EF) (residues 1-75),
 209 the N-terminal transmembrane domain of E protein (ET) (residues 1-39), and the C-terminal cytoplasmic domain

210 of E protein (EC) (residues 36-75). Two additional residues, GlySer, are present at the N-termini of all E protein
211 constructs. (C) Block diagram of the expression and purification protocols applied to the polypeptide sequences
212 shown in part B. (D) Example of SDS-PAGE at various stages of the expression and purification of EF: lane 1,
213 pre-induction cells; lane 2, post-induction cells; lane 3, HPC-solubilized inclusion bodies containing the KSI-EF
214 fusion protein; lane 4, Ni-affinity column flow through; lane 5, eluate of the KSI-EF fusion protein from the column;
215 lane 6, after thrombin cleavage of the KSI-EF fusion protein; lane 7, arrow marks the single band of purified EF
216 used in samples for the NMR experiments.

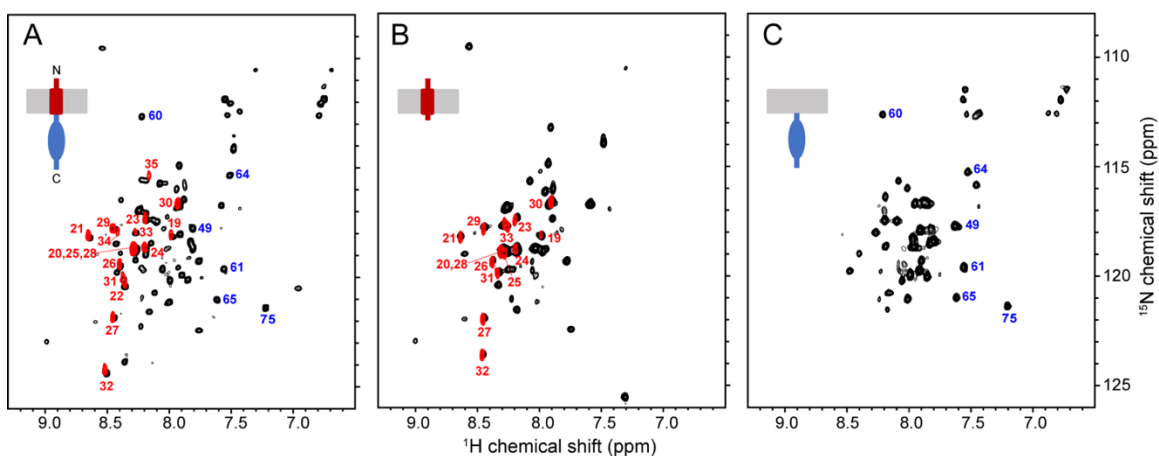
217 **Conformations of SARS-CoV-2 E protein domains are preserved**

218 Fig 3 compares $^1\text{H}/^{15}\text{N}$ HSQC spectra of three E protein constructs in HPC micelles. The spectra are
219 well-resolved despite the relatively narrow span of ^1H amide chemical shift frequencies (< 2 ppm)
220 consistent with the predominantly helical conformations observed previously [9, 17, 18]. The backbone
221 resonances of full-length E protein have been assigned and their chemical shifts deposited in the
222 Biological Magnetic Resonance Data Bank (accession number: 50813) (S3 Fig and S1 Table). Notably,
223 the observation of the expected number of resonances, with no evidence of doublings or unusual line
224 shapes from the selectively ^{15}N -Leu and ^{15}N -Val labeled samples (S4 Fig), where there are no
225 ambiguities due to spectral overlap, confirms chemical purity and conformational homogeneity of the
226 full-length protein in HPC under the experimental conditions. Any evidence of detergent-induced
227 structural perturbations or heterogeneous aggregation detected in these spectra would call for further
228 sample optimization before moving forward with solution NMR experiments or the initiation of the
229 preparation of bilayer samples for solid-state NMR experiments.

230 The spectra of the N-terminal transmembrane helix-containing domain (ET) (residues 1-39) (Fig
231 3B) and the C-terminal cytoplasmic domain (EC) (residues 36-75) (Fig 3C) are superimposable on the
232 spectrum of the full-length protein (EF) (residues 1-75) (Fig 3A), with the exception of signals from
233 residues proximate to the newly formed C-terminus of ET and N-terminus of EC (S5 Fig). These results
234 demonstrate that the folded structures of the domains are not perturbed by separation from each other,

235 which suggests an absence of inter-domain interactions and possibly independence of their biological
236 activities, which remains to be demonstrated *in vivo*.

237 Hydrogen/deuterium (H/D) exchange is an effective way to identify residues in transmembrane
238 helices of membrane proteins [46]. When samples of the E protein constructs were prepared in >90%
239 D₂O instead of ~ 90% H₂O, no amide signals from residues 36-75 in the cytoplasmic domain were
240 observable in the spectra of EF or EC; by contrast, strong signals from residues 19-35 and 19-33 were
241 present in the spectra of EF and ET, respectively (Fig 3 and Fig 4C), demonstrating that these residues
242 contribute to the stable core of its unusually long trans-membrane helix. Truncation at residue 39
243 enhances solvent exchange at residues 34 and 35 of ET, which are 5 and 6 residues distal to its C-
244 terminus, respectively, due to structural changes reflected in chemical shift changes of the resonances
245 from the nine terminal residues (S4C Fig).



247 **Fig 3. Comparison of ¹H/¹⁵N HSQC spectra of uniformly ¹⁵N-labeled E protein constructs in HPC micelles**
248 **in H₂O (black contours) and D₂O (red contours).** (A) Full-length E protein (EF) (residues 1-75). (B) N-terminal
249 transmembrane domain of E protein (ET) (residues 1-39). (C) C-terminal cytoplasmic domain of E protein (EC)
250 (residues 36-75). For reference, cartoons of each construct are shown. The assignments of selected resonances
251 are marked to distinguish among signals from ET (red numbers) and EC (blue numbers).

252 **Secondary structure and dynamics of full-length E protein in HPC micelles**

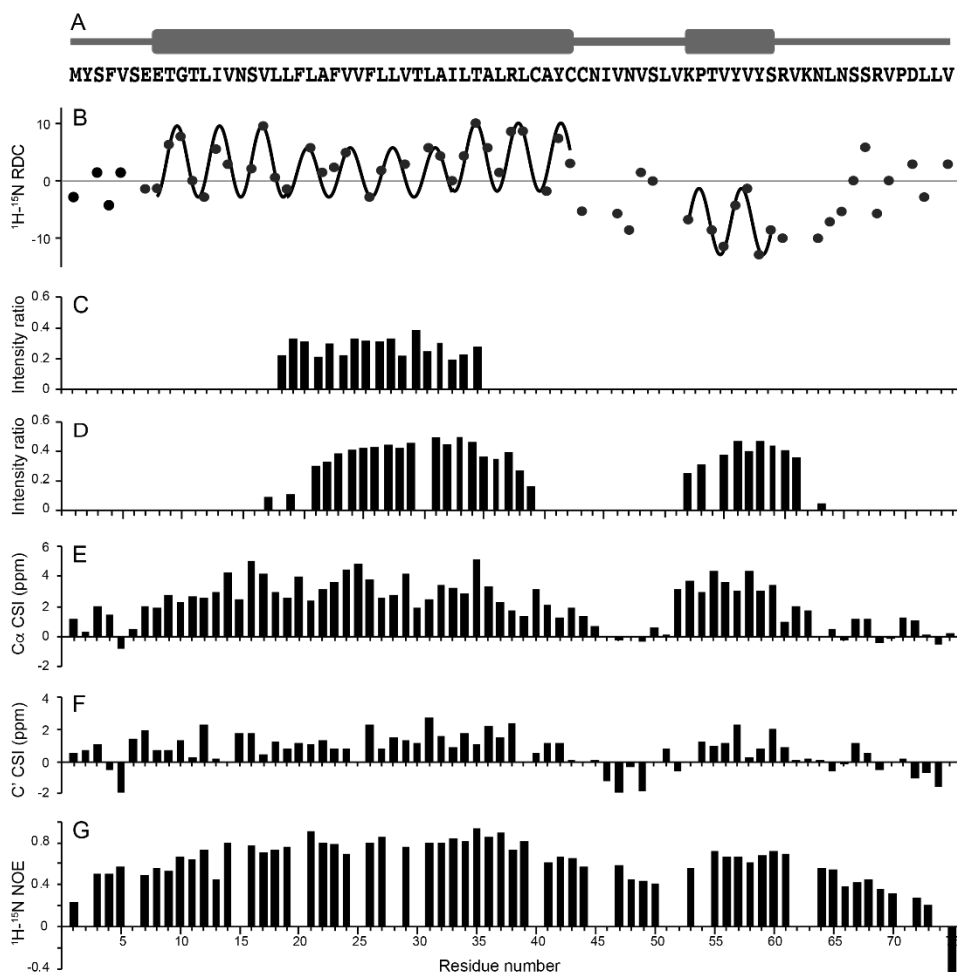
253 In previous studies, evidence has been presented that the predominant secondary structure of E
254 protein is α -helix. However, the lengths of the proposed helical segments varied widely, depending
255 upon which residues were included in the polypeptide constructs, the types of samples, and the
256 experimental conditions [9, 10, 17, 18]. Here we describe the secondary structure of full-length E
257 protein in HPC micelles by analyzing the chemical shifts of backbone ^{13}C resonances [47] and amide
258 $^1\text{H}/^{15}\text{N}$ residual dipolar couplings (RDCs) [48, 49]. Further support comes from H/D exchange,
259 manganese titration, and heteronuclear $^1\text{H}/^{15}\text{N}$ NOE measurements backed up by preliminary solid-
260 state NMR spectra of protein-containing phospholipid bilayers. Complementary results have been
261 obtained from samples of EF, ET, and EC.

262 Both the ^{13}C chemical shift index (CSI) plots (Fig 4C and 4D) and the $^1\text{H}-^{15}\text{N}$ dipolar wave plot (Fig
263 4B) demonstrate that full-length E protein has a long 36-residue transmembrane helix and a separate
264 short 8-residue cytoplasmic helix. None of these backbone data indicate the presence of regular
265 secondary structure in residues 43-52 located in the region linking the two helices. Although the RDCs
266 have significant amplitudes, as expected for a structured region, the $^1\text{H}/^{15}\text{N}$ heteronuclear NOE data
267 (Fig 4E) suggests that this well-defined internal region of the protein undergoes modest
268 amplitude/frequency motions that are not present in the helical regions. The $^1\text{H}/^{15}\text{N}$ heteronuclear NOE
269 data also shows that residues 2-7, before the start of the N-terminal helix, and residues 61-75 following
270 the end of the C-terminal helix exhibit gradients of increasing motion towards the termini, although even
271 the terminal residues do not appear to be highly mobile and unstructured, as is sometimes the case in
272 this class of proteins [32, 50].

273 The sinusoidal waves that fit best to the magnitudes and signs of the measured RDCs as a
274 function of residue number have a periodicity of 3.6 residues per turn, proving with a very high level of
275 confidence that the protein has segments of regular α -helix secondary structure [48, 49, 51]. The
276 addition or subtraction of a single residue at either end of the helical segments significantly degrades
277 the quality of the fit, providing a clear demarcation of the length of the helical segments. The different

278 average amplitudes of the two distinct dipolar waves in Fig 4B show that the two helices have different
279 orientations relative to the direction of molecular alignment. Another notable feature is that the dipolar
280 wave for the core region of the transmembrane helix (residues 19-34) is best fit by a sine wave with a
281 somewhat smaller amplitude than for the rest of the long helical region (residues 8-18 and 35-43),
282 suggesting that the 36-residue helix is not completely uniform throughout its length.

283 To assess the orientation of the C-terminal helix and possible interactions of the cytoplasmic
284 domain with the hydrophilic headgroups of HPC, we examined the effects of adding paramagnetic
285 manganese ions to samples of full-length E protein. Broadening of many $^1\text{H}/^{15}\text{N}$ HSQC resonances was
286 observed as a function of increasing the concentration of MnCl_2 . Significantly, the signals from residues
287 1-16, 40-51, and 64-75 were broadened beyond detection at a concentration of 5 mM MnCl_2 , while the
288 signals from residues 17-39 and 52-63 remained readily observable. These signals correspond almost
289 exactly to the residues in the core of the long hydrophobic helix (Fig 4B, 4C, and 4D) and the short
290 cytoplasmic helix, with the later suggesting that the cytoplasmic helix may interact with the membrane
291 surface.



292

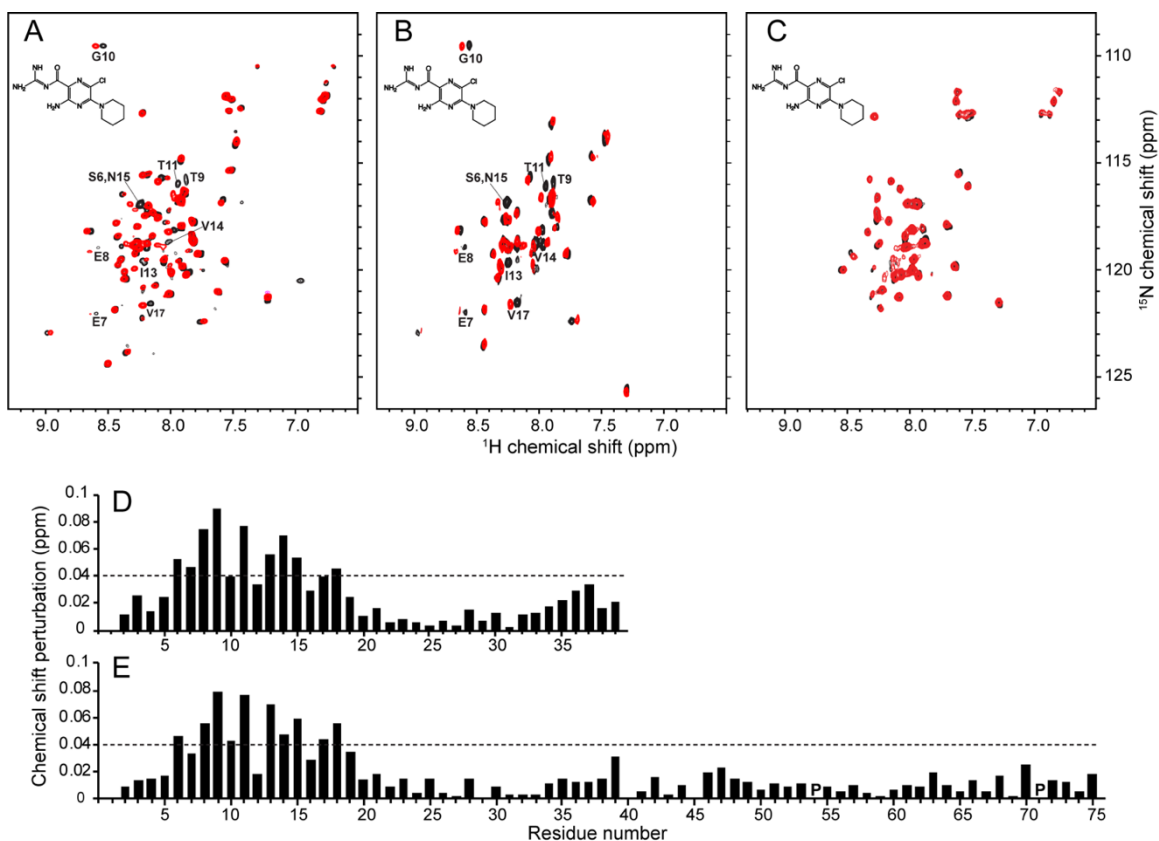
293 **Fig 4. Summary of NMR data obtained on full-length E protein in HPC micelles at 50°C.** (A) Schematic
294 representation of the distribution of helical segments (thick bars) above the corresponding amino acid residues of
295 E protein. (B) Plot of residual ^1H - ^{15}N residual dipolar couplings as a function of residue number. Fits to sine waves
296 with a periodicity of 3.6 reveal the dipolar waves characteristic of alpha helical secondary structure. The residual
297 dipolar couplings were measured on a weakly-aligned sample as shown in S6 Fig. (C) Ratios of resonance
298 intensities with the protein in D_2O compared to those in H_2O solution. (D) Ratios of resonance intensities in the
299 presence and absence of MnCl_2 . (E and F) Chemical shift index plots of alpha (E) and carbonyl (F) carbon
300 resonances, respectively. (G) Plot of ^1H - ^{15}N heteronuclear NOEs as a function of residue number.

301 Interactions of SARS-CoV-2 E protein with amilorides

302 The chemical shift perturbations (CSPs) in the $^1\text{H}/^{15}\text{N}$ HSQC spectra of the three E protein constructs
303 (EF, ET, and EC) caused by the addition of a ten-fold molar excess of hexamethylene amiloride (HMA)
304 to the samples are illustrated in Fig 5. The black contours represent the protein signals in the absence

305 and the red contours in the presence of HMA. For the constructs that include the N-terminal portion of
306 the protein, EF and ET, the chemical shifts of the corresponding residues were perturbed in the same
307 directions and to a similar extent, as illustrated in the plots of the chemical shift changes as a function
308 of residue number in Figs 5D and 5E. By contrast, no significant chemical shift changes were observed
309 in the resonances from the cytoplasmic domain (EC) alone (Fig 5E) or as part of the full-length protein
310 (EF) (Fig 5A). Although there is evidence that residues 2-5 are affected by drug binding, the most
311 strongly perturbed signals are associated with residues 6-18 at the N-terminal end of the long helix and
312 extending to the core portion distinguished by its resistance to H/D exchange and broadening by
313 manganese ions, as well as the reduced amplitude of its dipolar wave. Qualitatively, the data in Fig 5
314 confirm that HMA interacts with the N-terminal domain of E protein.

315 The EF and ET constructs were designed to include all N-terminal residues, and these data show
316 that the binding site definitely includes residues 6, 7, an 8, and likely residues 2, 3, 4 and 5, none of
317 which were present in the previously studied constructs, and extends to residue 18. Nearly all of the
318 residues that constitute the binding site belong to the highly regular helix, until it abruptly changes tilt
319 angles at residue 18, the start of the core region. The residues between Ser6 and Leu18 are perturbed
320 by binding HMA and undergo facile H/D exchange: resistance to H/D exchange starts with residue 18.
321 Notably, signals from four hydrophilic residues (Glu8, Thr9, Thr11, and Asn15) as well as Ile13 are
322 most perturbed by HMA binding. Smaller CSPs observed in the C-terminal region of ET were not
323 present with EF, which may be due to non-specific HMA binding to the unnatural exposed C-terminal
324 region of ET. Titration of ET with HMA results in gradual chemical shift changes (data not shown),
325 demonstrating that binding occurs in fast exchange on the timescales defined by the chemical shift
326 differences.

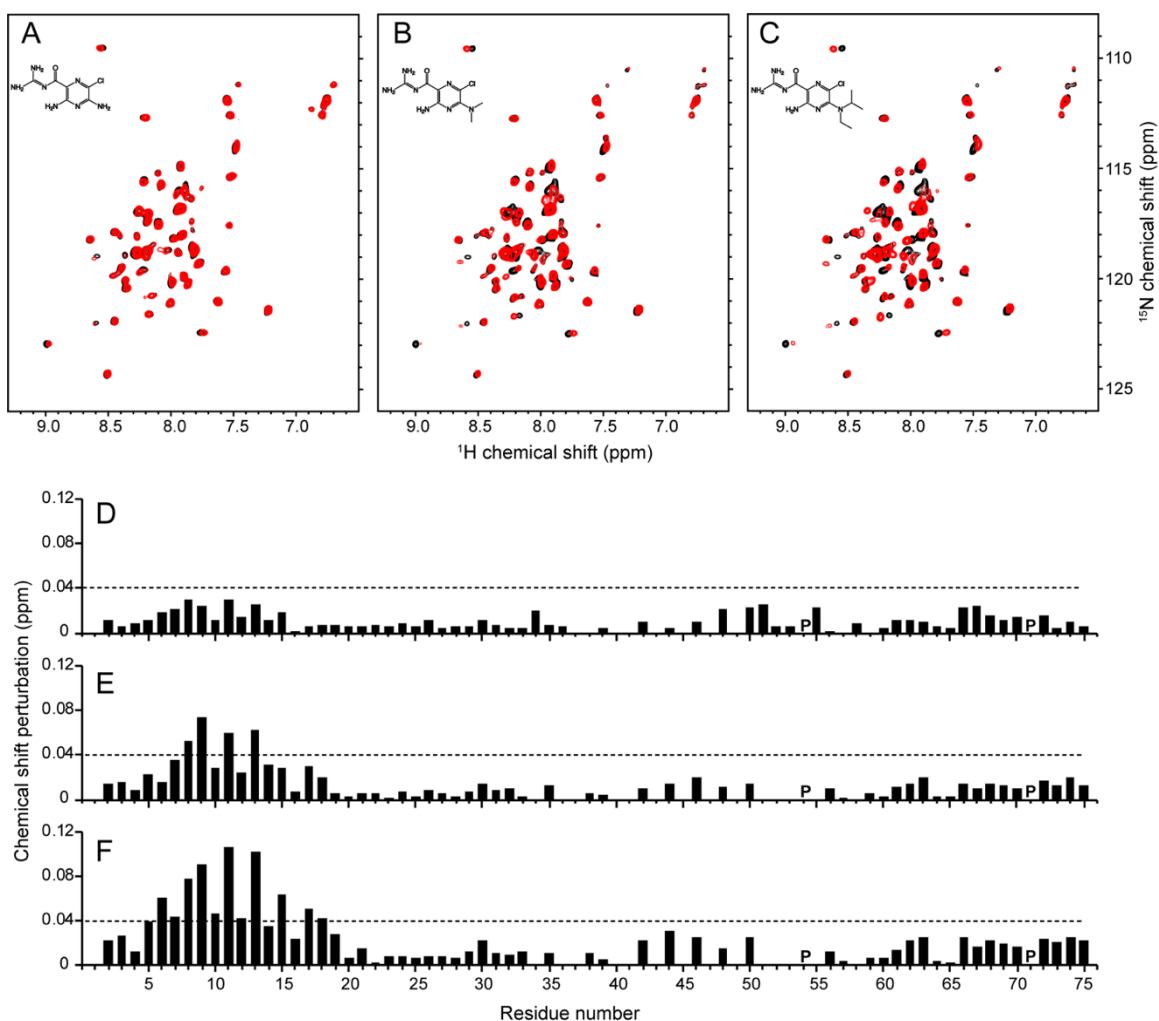


327

328 **Fig 5. Chemical shift perturbations resulting from HMA binding to E protein constructs in HPC micelles.**
329 (A-C) Superposition of $^1\text{H}/^{15}\text{N}$ HSQC NMR spectra of uniformly ^{15}N -labeled E protein constructs in the absence
330 (black contours) and presence (red contours) of HMA. (A) Full-length E protein (EF) (residues 1-75). (B) N-
331 terminal transmembrane domain of E protein (residues 1-38) (ET). (C) C-terminal cytoplasmic domain of E protein
332 (residues 39-75) (EC). The molar ratio of protein to HMA is 1:10. The chemical structure of HMA is shown in each
333 spectrum. The resonances perturbed by binding HMA are labeled with their assignments. (D and E) Plots of
334 chemical shift perturbations as a function of residue number of ET (D) and EF (E) derived from the NMR spectra
335 in B. and A., respectively. The horizontal dotted lines represent 1.5 times the average chemical shift perturbations
336 induced by HMA binding to ET. Proline sites are marked as "P".

337 To compare the binding sites and affinities, we added increasing amounts of amiloride and two
338 amiloride derivatives, dimethyl amiloride (DMA) and ethyl isopropyl amiloride (EIPA), to samples of full-
339 length E protein (EF) and monitored their two-dimensional $^1\text{H}/^{15}\text{N}$ HSQC spectra (Fig 6). Notably, the
340 same residues of EF were affected by all of the amiloride derivatives albeit with different magnitudes of
341 CSPs, indicating that they all utilize the same binding site but with different binding affinities. No
342 significant changes were observed to the EF spectrum upon addition of amiloride (Fig 6A and 6D),

343 while the largest changes were observed with EIPA (Fig 6C and 6F), DMA induced moderate changes
344 and the magnitudes of its CSPs lie between those of amiloride and HMA (Fig 6B and 6E). The
345 magnitudes of the CSPs indicate that the order of binding affinities to E protein is EIPA \approx HMA > DMA
346 >> amiloride.

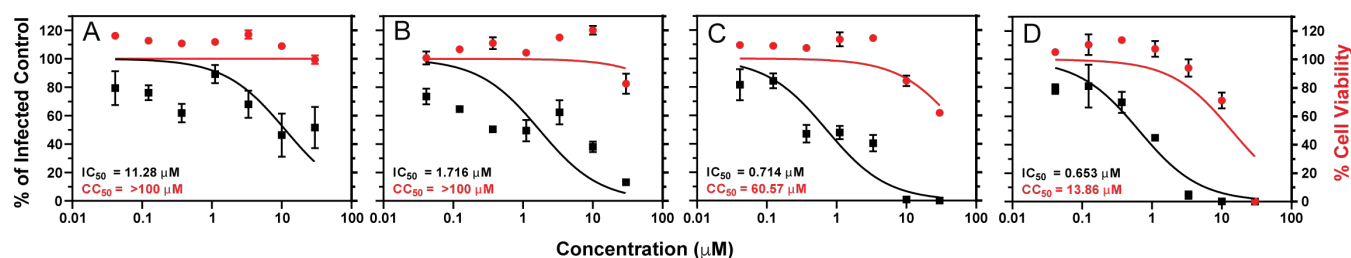


347

348 **Fig 6. Comparison of interactions of E protein with amiloride compounds.** (A-C) $^1\text{H}/^{15}\text{N}$ HSQC NMR spectra
349 of uniformly ^{15}N -labeled full length E protein (EF) in the absence (black contours) and presence (red contours) of
350 (A) amiloride, (B) DMA, and (C) EIPA. The molar ratio of EF to each compound is 1:10. Chemical structures of the
351 drugs are shown in the spectra. (D-F) Plots of chemical shift perturbations (CSPs) in the presence of (D)
352 amiloride, (E) DMA, and (F) EIPA as a function of residue number. The dotted lines indicate 1.5 times the average
353 chemical shift changes of EF by EIPA. Proline sites are marked as "P".

354 **Antiviral activity of amilorides against SARS-CoV-2**

355 The amiloride derivatives were tested for their ability to inhibit replication of SARS-CoV-2 in Vero E6
356 cells. Mirroring the NMR binding data of E protein in Figs 5 and 6, the compounds with bulkier aliphatic
357 or aromatic substituents at the 5' pyrazine ring (EIPA and HMA) showed the strongest inhibition, with
358 sub-micromolar IC_{50} values, while the compounds with smaller substituents were less effective
359 inhibitors (Fig 7). The similarity of the trends for inhibition of replication and of binding to E protein
360 suggests that this protein may very well be a target for the antiviral activity of amiloride compounds. Of
361 note, the most active compound examined here, HMA, shows considerable cytotoxicity (therapeutic
362 index = 21.23), therefore, EIPA may be a better choice for potential therapeutic use (therapeutic index
363 = 84.83) or as a starting point for further drug development.

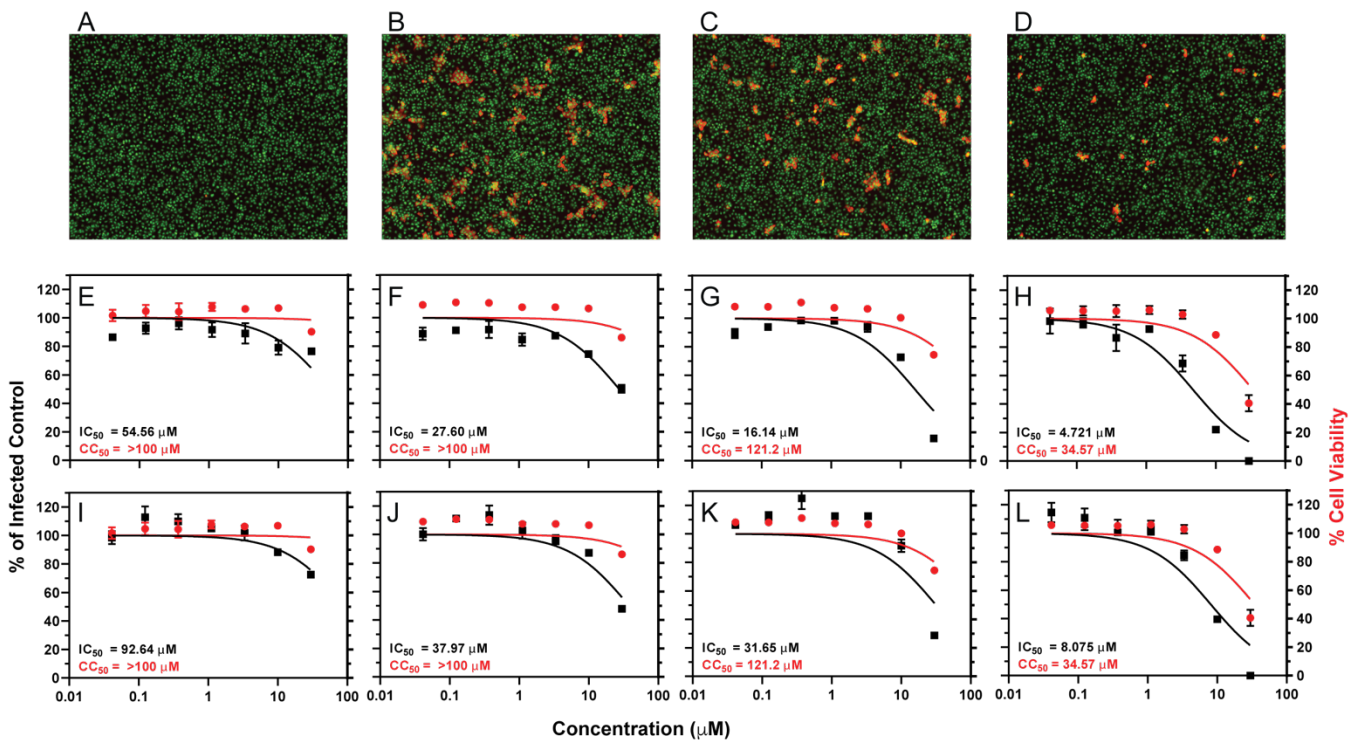


364
365 **Fig 7. Inhibition of SARS-CoV-2 infection by amiloride compounds in Vero E6 cells infected at low MOI**
366 **and incubated for 48 hours.** IC_{50} and CC_{50} curves of (A) amiloride, (B) DMA, (C) EIPA, (D) HMA. The
367 compounds were added at the indicated concentrations to Vero E6 cells simultaneously with authentic SARS-
368 CoV-2 virus (MOI 0.1) and incubated for 48 hours. Inhibition of infection (solid squares and curves in black) was
369 measured by high-content imaging for intracellular SARS-CoV-2 N protein and is relative to a DMSO-treated
370 infected control. Cytotoxicity (solid circles and curves in red) was measured similarly using a nuclei stain and
371 quantifying cell numbers relative to the DMSO-treated infected control. The curves were calculated using the
372 nonlinear regression analysis in GraphPad Prism 9. IC_{50} and CC_{50} values for each compound are indicated in the
373 plots.

374 In order to identify the stage of the viral replication cycle affected by the amiloride compounds, their
375 antiviral activity was reevaluated at a high multiplicity of infection (MOI of 1.0 infectious units per cell)
376 and after a relatively brief incubation (Fig 8, 18 hours). The same ranking of antiviral activity among the
377 compounds was observed, with HMA and EIPA the most active. The observed IC_{50} values were higher
378 than those measured in the experiments summarized by the data shown in Fig 7. This was not
379 unexpected since the antiviral assay of Fig 8 was done at an MOI ten-fold higher than that of Fig 7, and

380 the time of incubation allowed for only one or two replication cycles (18 hours in Fig 8 compared to 48
381 hours in Fig 7). We observed microscopically that EIPA and HMA decreased the number of cells in
382 each infected focus in the monolayer (Fig 8C and 8D). This effect was especially striking for HMA; most
383 foci contained only one or two cells, suggesting that the spread of infection to adjacent cells in the foci
384 was inhibited. To determine whether the amiloride compounds were inhibiting only this cell-cell spread
385 or were also affecting the infectivity of the inoculum, we enumerated both the number of infected cells
386 and the number of infected-cell-foci (containing one or more cells) and compared the IC₅₀ values
387 obtained with each (Fig 8). The IC₅₀ values obtained using the number of infected cells (Fig 8E-8H)
388 were less than those obtained using the number of infected-cell-foci (Fig 8I-8L). These data suggest
389 that the amiloride compounds act late in the viral replication cycle and affect the spread of virus from
390 cell-to-cell, although they do not exclude the possibility of a modest effect on the establishment of
391 infection by cell-free virus.

392



393

394 **Fig 8. Inhibition of SARS-CoV-2 infection by amiloride compounds in Vero E6 cells infected at high MOI and**
395 **incubated for 18 hours.** (A-D) Images of cells. Green: nuclear stain (Sytox green); red: stain for nucleocapsid (N)
396 using an antibody conjugated to AlexFluor594. (A) Uninfected cells. (B-D) Infected with SARS-CoV-2 and treated
397 with (B) 0.1% DMSO, (C) 10 μ M EIPA, and (D) 10 μ M HMA. (E-L) IC₅₀ and CC₅₀ curves of (E and I) amiloride, (F
398 and J) DMA, (G and K) EIPA, and (H and L) HMA for total infected cells (E-H) and foci of infection (I-L). The
399 compounds were added at the indicated concentrations to Vero E6 cells simultaneously with SARS-CoV-2 (MOI 1)
400 and incubated for 18 hours. Inhibition of infection (solid squares and curves in black) was measured by high-content
401 imaging for intracellular SARS-CoV-2 N protein and is relative to a DMSO-treated infected control. Cytotoxicity
402 (solid circles and curves in red) was measured similarly using a nuclei stain and quantifying cell numbers relative
403 to the DMSO-treated infected control. The curves were calculated using the nonlinear regression analysis in
404 GraphPad Prism 9. IC₅₀ and CC₅₀ values for each compound are indicated in the plots.

405 **N15A and V25F mutations of E protein affect VLP production**

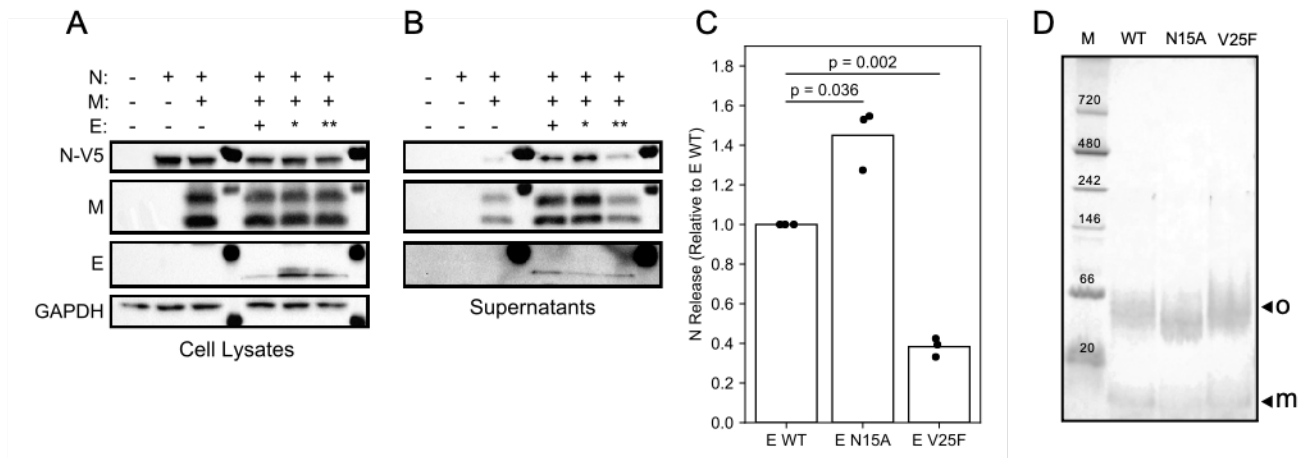
406 Co-expression of the structural proteins M and N of SARS-CoV-2 in HEK293T cells results in a modest
407 release of N-containing virus-like particles (VLPs) judging by the intensity of the N protein band in
408 western blots of culture supernatants after centrifugation through a sucrose cushion. Notably, the added
409 expression of wild-type E protein greatly stimulated the release of VLPs (Fig 9A and 9B).

410 Previous studies of E protein of Infectious Bronchitis Virus (IBV), a gamma coronavirus, showed
411 that mutations within the transmembrane domain altered the ability of VLPs to assemble [52]. To
412 determine the impact of similar mutations in SARS-CoV-2 E protein, two mutants were generated,
413 N15A and V25F, which are analogous to IBV E protein residues Thr16 and Ala26, respectively (S1 Fig).
414 The N15A and V25F mutations in SARS-CoV-2 E protein increased their expression compared to the
415 wild-type protein in HEK293T cell lysates (Fig 9A). Similar to the T16A mutation in IBV E protein, the
416 N15A mutation in SARS-CoV-2 E protein increased VLP production by approximately 40% compared to
417 the wild-type E protein, while the V25F mutation decreased VLP production by 60% compared to wild-
418 type E protein, similar to the effect of the A26F mutation on the IBV E protein (Fig 9B and 9C).

419 The mutations T16A and A26F in the IBV E protein have been shown to affect its oligomeric state
420 [52]. However, the analogous mutations in the SARS-CoV-2 E protein do not appear to affect its

421 oligomerization *in vitro* under our experimental conditions; in PFO-PAGE, both of these mutant E
 422 proteins ran as oligomers with only slightly different migration patterns compared to the wild-type
 423 protein (Fig 9D). As expected, both of the mutant proteins ran as monomers in SDS-PAGE with their
 424 apparent molecular weights similar to that of the wild-type protein (data not shown).

425



426

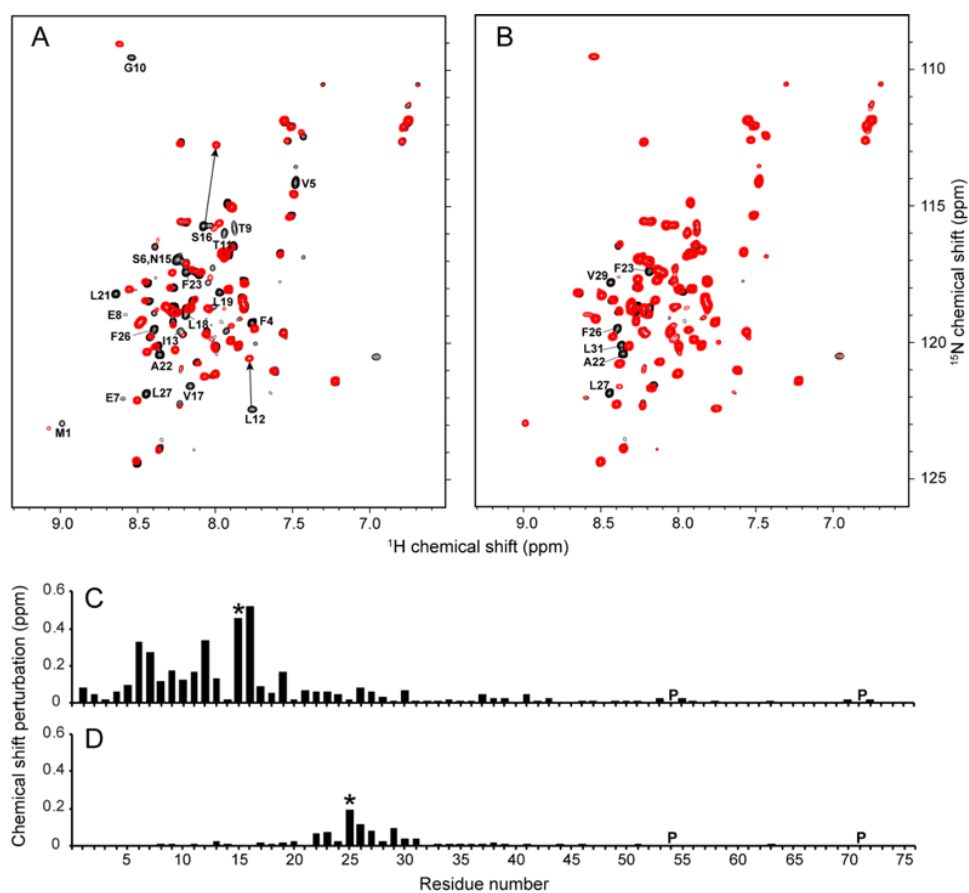
427 **Fig 9. Comparison of virus-like particle (VLP) production among wild-type and two mutant E proteins.** (A
 428 and B) Representative western blots of HEK293T cell lysates and sucrose cushion-purified supernatants following
 429 co-transfection with SARS-CoV-2 M, E, and N protein sequences, respectively. For E protein, * indicates the
 430 N15A mutant and ** indicates the V25F mutant. (C) Densitometry of the N protein band in purified supernatants
 431 from three independent western blot experiments. Each has M+N and the indicated E protein. The relative change
 432 over M+N without E protein is plotted for each condition. (D) PFO-PAGE of wild-type, N15A mutant, and V25F
 433 mutant E proteins. Monomer (m) and oligomer (o) bands are marked with arrows.

434 **Effects of N15A and V25F mutations on structure and HMA binding of E protein**

435 The N15A mutation results in significant chemical shift perturbations of resonances from residues
 436 throughout the N-terminal region of E protein, especially for the signals from Ser6, Glu7, Leu12, and
 437 Ser16 (Fig 10A and 10C). In contrast, only minor perturbations were observed for signals from residues
 438 adjacent to the mutation site in the V25F mutant E protein (Fig 10B and 10D). Since no significant
 439 differences were observed among the circular dichroism spectra from wild-type E protein and these two

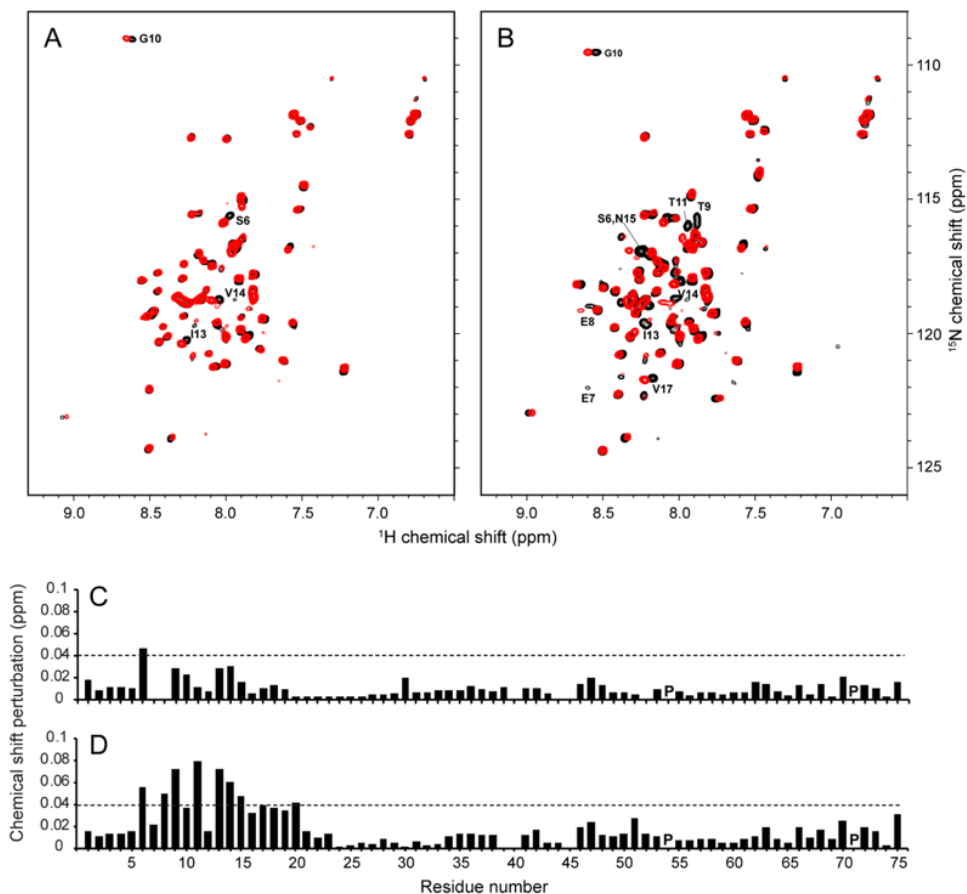
440 mutant proteins (data not shown), the relatively large and wide spread chemical shift perturbations by
441 the N15A mutation may result from changes in intermolecular hydrogen bonding involving Asn15 side
442 chains [53].

443 Previous mutational studies of polypeptides containing the transmembrane helix of SARS-CoV E
444 protein have shown that a single mutation, e.g., N15A or V25F, can disrupt ion channel activity in lipid
445 bilayers [54, 55]. We found that the N15A mutation of SARS-CoV-2 E protein decreased HMA binding,
446 since no significant chemical shift changes are observed in the presence of HMA, with the exception of
447 Ser6 (Fig 11A and 11C). By contrast, HMA binding was not affected by the V25F mutation, since the
448 chemical shifts of signals from residues near the HMA binding site were unchanged and their CSPs
449 were identical to those observed for wild-type E protein (Fig 11B and 11D). Based on these results, it
450 appears that Asn15 is essential for maintaining the conformation of E protein required for binding HMA.



451

452 **Fig 10. Comparison of NMR data of N15A and V25F mutants of E protein.** (A and B) $^1\text{H}/^{15}\text{N}$ HSQC NMR
453 spectra of N15A and V25F mutant E proteins (red contours) superimposed on those from the wild-type E protein
454 (black contours), respectively. The resonances that are significantly perturbed by the mutations are labeled with
455 their assignments. (C and D) Chemical shift perturbation plots for the N15A and V25F mutants of E protein,
456 respectively. The mutation sites are indicated with asterisks and the proline sites are marked as “P”.



457

458 **Fig 11. Comparisons of the effects of HMA binding on the NMR spectra of N15A and V25F mutants of E**
459 **protein.** (A and B) $^1\text{H}/^{15}\text{N}$ HSQC NMR spectra of N15A and V25F mutants of E protein in the absence (black
460 contours) and presence (red contours) of HMA, respectively. Significantly perturbed resonances by HMA are
461 labeled with their assignments. (C and D) Chemical shift perturbation plots of the effects of HMA binding to the
462 N15A and V25F mutants of E protein, respectively. The dotted lines indicate 1.5 times the average chemical shift
463 changes of V25F EF by HMA. Proline sites are marked as “P”.

464 Discussion

465 The coronavirus SARS-CoV-2 presents formidable challenges to human health, virology, and structural
466 biology. Structural and functional studies of the envelope (E), spike (S), and membrane (M) proteins are
467 especially challenging because, as shown in Fig 1, significant portions of these proteins reside within
468 the phospholipid bilayer of the viral envelope. Here we combine the results of solution NMR
469 spectroscopic studies and virologic studies of SARS-CoV-2 E protein to evaluate its potential as a drug
470 target. We focused our studies on the 75-residue full-length E protein and two overlapping truncated
471 constructs corresponding to the N-terminal transmembrane domain (residues 1-39), that includes a
472 long hydrophobic helix, and the C-terminal cytoplasmic domain (residues 36-75), that includes a short
473 helix and three cysteine residues (Fig 2B).

474 Heterologous expression of viral membrane proteins in *E. coli*, the most convenient system for the
475 preparation of milligram amounts of isotopically labeled proteins, is generally problematic. Hydrophobic
476 membrane proteins are prone to aggregation, likely from non-specific hydrophobic intermolecular
477 interactions or possibly incorrect intra- and/or inter- molecular disulfide linkages, the latter of which is
478 especially pertinent for SARS-CoV-2 E protein because it has three closely spaced cysteine residues in
479 its C-terminal domain. The expression of full-length E protein from SARS-CoV, whose sequence is
480 nearly identical to that of the 75-residue protein from SARS-CoV-2, has been reported [44]; however, a
481 modified β -barrel construct was used as the expression tag along with urea to solubilize the inclusion
482 bodies, followed by chemical cleavage and HPLC purification. The resulting protein in DPC or mixed
483 DPC/SDS micelles did not yield NMR spectra suitable for structural studies. Essentially all previous
484 NMR studies of SARS-CoV-2 E protein [9, 10, 17, 18] were carried out on substantially smaller
485 polypeptides with either 31 or 58 residues. In addition to the smaller number of residues in the
486 polypeptides and the missing N- and C- terminal amino acids, the prior studies differ from those
487 described here in several other substantial ways, including the expression system, choice of fusion
488 protein, method of protein expression and purification, choice of micelle-forming detergent, and other

489 experimental parameters. Not surprisingly, there are many significant differences between the findings
490 of the previous NMR studies and those described here. Moreover, we carried out spectroscopic and
491 virologic studies in parallel, with the results of both serving as controls, suggesting subsequent
492 experiments and guiding the interpretation of the findings.

493 Nothing could be done without the preparation of isotopically labeled E protein samples suitable for
494 NMR spectroscopy. This formidable barrier required the design and implementation of a novel bacterial
495 expression and purification system (Fig 2). There are three notable aspects to our approach: 1) The
496 KSI-E protein fusion protein expression system in C43(DE3) *E. coli* cells boosts expression levels and
497 circumvents cytotoxicity by sequestering the overexpressed hydrophobic E protein in inclusion bodies;
498 2) Insertion of a 24-residue linker, which includes a ten-His tag and a 6-residue (LVPRGS) thrombin
499 cleavage site, between the sequences of the KSI and E proteins, facilitates affinity chromatography
500 purification and enzymatic cleavage because thrombin retains specificity and activity at low detergent
501 concentrations; 3) A single “mild” detergent, HPC, with low CMC, is used to solubilize the protein
502 throughout all steps of isolation, purification, and sample preparation. This eliminates the need for
503 detergent or lipid exchanges and is applicable to full-length, truncated, and mutated constructs of E
504 protein (Figs 3 and 9). Moreover, this approach to sample preparation may be generally applicable to
505 other membrane proteins. We have already used it to prepare samples of several constructs of the
506 membrane binding domain of the SARS-CoV-2 Spike protein (Fig 1) that yield high-resolution NMR
507 spectra (data not shown). In addition, this approach provides an expedient starting point for the
508 preparation of samples of E protein and potentially other membrane proteins in liquid crystalline
509 phospholipid bilayers at the high lipid to protein ratios required for solid-state NMR spectroscopy under
510 near-native conditions. Initial comparisons between results obtained in HPC micelles by solution NMR
511 and those obtained in phospholipid bilayers by oriented sample solid-state NMR (S7A Fig) provide
512 assurance that the protein structure is not strongly affected by HPC. This is significant because there
513 have been no previous NMR studies of membrane proteins in HPC micelles. The feasibility of solution

514 NMR studies of full-length SARS-CoV-2 E protein is demonstrated by the high-resolution and signal-to-
515 noise ratios of resonances from individual amide sites in the two-dimensional $^1\text{H}/^{15}\text{N}$ NMR spectrum of
516 a uniformly ^{15}N labeled sample (Fig 3A). This includes the assignment of backbone resonances using
517 standard triple-resonance methods [56] on a uniformly ^{13}C - and ^{15}N - double-labeled sample. Following
518 the sequential assignment of all backbone resonances in the spectra of three overlapping E protein
519 constructs, EF (residues 1-75), ET (residues 1-39), and EC (residues 36-75), it was straightforward to
520 characterize the overall organization, secondary structure, and local dynamics of E protein in HPC
521 micelles using the set of experimental data aligned by residue number in Fig 4. The most striking
522 feature to emerge is that E protein has a very long 36-residue α -helix (residues 8-43) in the N-terminal
523 transmembrane domain. There is also a shorter 8-residue α -helix (residues 53-60) in the C-terminal
524 domain that has a different orientation in the protein than the long helix. Since the ^1H and ^{15}N chemical
525 shifts of the vast majority of resonances present in the two-dimensional HSQC spectra (Fig 3) of the
526 full-length and truncated constructs overlap nearly exactly, the conformations of the N-terminal and C-
527 terminal domains are the same whether alone or as part of the intact protein. The conservation of
528 domain structures, also observed for the small membrane protein Vpu from HIV-1 [31, 57], suggests
529 that each domain of E protein has separate roles in the virus life cycle, although this remains to be
530 shown in future *in vivo* experiments.

531 Prior NMR studies have shown E protein to be largely helical. However, the polypeptides used in
532 the experiments and the model membrane environments differ so much that it is premature to provide a
533 comprehensive analysis of why the lengths, locations, and distortions of the helical segments differ so
534 drastically among various reports [9, 10, 17, 18]. As an example, in 2009 Pervushin et al. [17] found by
535 NMR that all 31 residues of a synthetic polypeptide with a sequence corresponding to residues 8-38 of
536 E protein participated in a continuous α -helix in the presence of DPC. By contrast, in a 2020 report
537 Mandala et al. [10] found by NMR a 21- or 25-residue helix, with a substantial local distortion, in the
538 same polypeptide prepared by bacterial expression, in the presence of DMPC instead of DPC.

539 Here we make direct comparisons between our results on the 75-residue full-length E protein and
540 those in the most recent report, cited above, on the widely used 31-residue doubly truncated
541 polypeptide [10]. We find that the 36-residue transmembrane helix is quite long (residues 8-43 of the
542 full-length E protein) compared to the more typical 21- or 25- residue transmembrane helix found by
543 Mandala et al. The results also differ regarding the distortion of this helix. We find it to be continuous
544 and straight, with the exception of the 17-residue core (residues 19-35), identified by resistance to H/D
545 solvent exchange and broadening by the presence of paramagnetic Mn^{2+} in the solution, and most
546 definitively by the dipolar wave analysis that shows that this segment is also straight albeit with a
547 detectably different tilt angle than the co-linear N- and C-terminal portions of the helix (residues 8-18
548 and 36-43). Instead, Mandala et al. [10] describe a singular 4-residue distortion at residues 20-23.
549 Oriented sample solid-state NMR data (S7A Fig) shows that the membrane-spanning helix has a large
550 tilt angle (approx. 45°) as necessitated by hydrophobic matching of the 36-residue hydrophobic helix
551 with the 14-carbon methylene chains of DMPC bilayers [58] By contrast, Mandala et al. [10] interpret
552 their MAS solid-state NMR data to show that this helix has a very small tilt angle in the presence of
553 DMPC. On the one hand, our solid-state NMR experiments were performed on a uniaxially aligned
554 sample with the bilayer normal perpendicular to the direction of the magnetic field (S7A Fig), therefore
555 the protein must be undergoing rapid rotational diffusion at $35^\circ C$ in order to yield spectra with narrow
556 single-line resonances. On the other hand, Mandala et al. [10] state that the protein does not undergo
557 fast rigid-body uniaxial rotation at high temperatures. The differences between the structural findings in
558 the two studies may arise from a number of possible sources, such as the difference in the lengths of
559 the polypeptides (75 vs. 31 residues), properties of the membrane-like environments produced by HPC
560 and DMPC, and the use of different NMR approaches (primarily solution NMR complemented by a
561 contribution from OS solid-state NMR vs. MAS solid-state NMR). The PISA Wheel-based analysis [59,
562 60] of the solid-state NMR spectrum of uniformly ^{15}N labeled ET in aligned phospholipid bilayers (S7
563 Fig) shows that the transmembrane helix has a large tilt angle ($\sim 45^\circ$) that is consistent with the finding
564 of a very long (36-residue) trans-membrane helix in HPC micelles. The one-dimensional NMR spectrum

565 in S7 Fig as well as complementary two-dimensional PISEMA spectra (data not shown) foreshadow the
566 structure determination of SARS-CoV-2 E protein in phospholipid bilayers under near-native conditions.

567 Outstanding questions about E protein include whether it has *in vivo* ion channel activity, and
568 whether this activity is responsible for essential biological functions. Channel activity has been
569 observed for full-length E protein as well as N-terminal constructs containing its principal helix. This has
570 been used as evidence that it forms a pentamer with a central pore characteristic of viroporins. Since it
571 is small viral protein with 75 residues, it is classified as a miniprotein [16]. If its ion channel activity does
572 indeed result from forming a defined oligomer, then it can be categorized as a viroporin. However, its
573 primary and secondary structures differ dramatically from proteins previously described as viroporins.
574 Most notably, the 36-residue helix of the E protein is much longer than the trans-membrane helices
575 identified in archetypical viroporins like Vpu from HIV-1 [32] and M2 from influenza virus [61], whose
576 shorter transmembrane helices have 18- and 25- residues, respectively.

577 A hallmark of viroporins is that they form homo-oligomers in the host membranes and their
578 amphipathic transmembrane domain is essential for ion channel activity. The full-length E protein has a
579 monomeric molecular weight of 8.5 kDa. It migrates as an oligomer with an apparent molecular weight
580 of about 50 kDa with a minor band of monomers in PFO-PAGE (Fig 8D). The protein has three
581 cysteines (C40, C43, and C44) and at least two of them are conserved across α/β coronaviridae (S1
582 Fig). The presence of reducing agents does not affect the PFO-PAGE or the NMR spectra of E protein,
583 suggesting that cysteines are not involved in oligomerization or aggregation. Its existence in pentamers
584 is primarily attributed to results from detergent micelle-based analytical ultracentrifugation and BN-
585 PAGE and PFO-PAGE analysis [18, 44]. IBV E protein has also been shown to exist as both
586 monomers and oligomers during transient expression and infection by sucrose gradient analysis, and
587 its oligomers have been proposed to correlate with stimulation of VLP production [52]. As with most
588 other miniproteins, with the notable exception of M2 from influenza, the definition of E protein as a
589 viroporin remains controversial.

590 Ion-channel activity invites the use of established channel blocking compounds as experimental
591 probes. HMA has exhibited inhibitory activity against E protein ion channels from various
592 coronaviruses, including MHV, HCoV-229E, SCV and FIPV, with a low micromolar range of EC_{50} [30,
593 62] as well as Vpu from HIV-1 [63] and p7 from HCV [64]. Interactions of HMA with the transmembrane
594 domain of SARS-CoV E protein have been previously examined by NMR [9, 10, 17, 18], and different
595 drug binding sites have been proposed based on the chemical shift perturbations observed for different
596 truncated E protein constructs and experimental conditions. The chemical shift perturbations we
597 observe in spectra of 75-residue full-length SARS-CoV-2 E protein in Fig 5 provide a more complete
598 picture of its interactions with HMA than is possible with 31- or 58- residue polypeptides. In addition, the
599 comparison of chemical shift perturbations of three SARS-CoV-2 E protein constructs, EF, ET, and EC,
600 in the presence of HMA clearly demonstrates that N-terminal residues 2-18 are affected by binding
601 HMA. In our spectra, signals from hydrophilic residues (S6, E7, E8, T9, T11, and N15) are strongly
602 affected by HMA. Minor perturbations of signals from residues in the C-terminal end of the trans-
603 membrane helix (residues 35-37) were observed in ET but not in EF and EC and are likely due to
604 nonspecific interactions from the truncated site. This contrasts with a prior result obtained on a
605 truncated E protein construct with residues 8-65 that showed large CSPs for V49 and L65 [18]. A
606 dramatic illustration that caution must be used when drug binding sites are mapped using truncated
607 constructs is an early study of M2 [65].

608 A ten-fold molar excess of amiloride and its derivatives DMA, HMA, and EIPA affect resonances
609 from the same set of amino acid residues in SARS-CoV-2 E protein, demonstrating that they utilize the
610 same binding site. With different CSP magnitudes, they display different binding affinities. Amiloride
611 itself did not induce any significant changes, DMA induced modest changes, and HMA and EIPA
612 induced the largest changes. Notably, the order of affinity of the compounds, $EIPA \approx HMA > DMA \gg$
613 amiloride, correlates well with their partition coefficient (logP) values: EIPA, 1.3; HMA, 1.3; DMA, 0.1,
614 and amiloride, -0.7 (<https://pubchem.ncbi.nlm.nih.gov>). Therefore, introduction of bulky aliphatic or

615 aromatic moieties in the 5' position of the amiloride pyrazine ring, which increases the lipophilicity of the
616 compounds, appears to increase their binding affinity for E protein. Most significantly, these findings
617 correlate well with the antiviral activities observed for these compounds in cultures of Vero E6 cells
618 infected with SARS-CoV-2. These data provide additional support for E protein being the likely *in vivo*
619 target of these compounds, and they suggest that inhibition of the ion channel activity may suppress
620 virus replication. Notably, the activity of EIPA and HMA for the Na⁺/K⁺ ATPase is higher than of
621 amiloride [66]. Therefore, structure-based optimization of target-selectivity will be necessary in order to
622 develop an amiloride-based drug aimed at E protein.

623 E protein not only stimulates viral assembly and release but also alters the secretory pathway of
624 the cell in a manner that preserves the function of the Spike protein [67]. Consequently, while
625 attributing the antiviral activity of the amilorides to assembly and release functions is tempting, these
626 compounds might also impair the infectivity of virions by inhibiting the "S-preserving" function of E
627 protein. The activities of the amilorides shown here under the conditions of high-multiplicity infection
628 suggest that much of their antiviral action is at a late-event in the replication cycle, consistent with a
629 block to assembly and release. Nonetheless, we have not fully excluded an effect, albeit modest, on
630 the infectivity of cell-free virus. Such an effect would be consistent with a partial loss of S activity in
631 mediating viral entry into target cells.

632 High-order oligomerization of IBV E protein has been proposed as a requirement for virus
633 assembly [52]. Although we do not observe changes in oligomeric states of N15A or V25F mutant E
634 proteins under our experimental conditions, comparisons of their CSPs suggests that the N15A
635 mutation but not the V25F mutation causes a significant change in the N-terminal region. The N15A
636 mutation affects the entire binding site and abolishes the interaction with HMA, demonstrating that
637 residue N15 plays a key role in maintaining SARS-CoV-2 E protein's native conformation and its ability
638 to interact with HMA. N15 (or Q15) is highly conserved in alpha and beta coronavirus E proteins.
639 Moreover, a single Gln can mediate helix-helix associations through intermolecular hydrogen bonding

640 within transmembrane domains [68]. Intermolecular hydrogen bonds involving the sidechain of N15
641 may be essential for maintaining the conformation and orientation of the N-terminal region, a conclusion
642 also suggested by the pentameric model of the E protein oligomer [10]. The small CSPs induced by the
643 V25F mutation are localized near the mutation site indicating that the conformation of the mutant E
644 protein is preserved, which is consistent with its response to HMA being identical to that of the wild-type
645 E protein.

646 Interest in the structure and function of SARS-CoV-2 E protein motivated the development of an
647 efficient new approach to the expression and purification of membrane proteins so that the full-length
648 protein could be studied. We demonstrate that HMA and EIPA bind to the N-terminal region of the E
649 protein and exhibit antiviral activity against SARS-CoV-2. We also found that residue N15 plays an
650 important role in maintaining the conformation of the HMA binding site, providing insight that might be
651 helpful in the design of drugs targeting E protein. Changes associated with the N15A and V25F
652 mutations are suggestive of involvement of E protein's N-terminal domain in virus assembly and/or
653 release. These biological activities can be correlated with the secondary structure of E protein, which
654 consists of a long hydrophobic transmembrane helix with a large tilt angle between residues 8-43
655 separated by a slightly dynamic but still structured linker region to a second shorter helix between
656 residues 53-60 with a significantly different tilt angle. Determination of the three-dimensional structure
657 of E protein in phospholipid bilayers is an essential next step that should provide the structural
658 information required to not only understand the protein's biological functions more fully, but also
659 optimize interactions with compounds that have the potential to be developed into antiviral drugs.

660 **Materials and methods**

661 **Design of SARS-CoV-2 E protein constructs**

662 All of the studies described here utilized polypeptides with sequences based on that of the wild-type 75-
663 residue full-length E protein from the SARS-CoV-2 isolate Wuhan-Hu-1 (NC_045512) (Fig 2B). To

664 enhance the expression of the viral E protein in *E. coli*, a codon-optimized gene for its amino acid
665 sequence was synthesized using the codons of highly expressed *E. coli* genes (S2 Fig)
666 (www.idtdna.com). The codon-optimized gene was inserted into a modified pET-31b(+) vector
667 (www.emdmillipore.com) and expressed as a ketosteroid isomerase (KSI)-fusion protein. A twenty-four-
668 residue linker sequence incorporating a 10 His-tag and a 6-residue (LVPRGS) thrombin cleavage site
669 was inserted between the KSI and E protein sequences (Fig 2A). The same expression and purification
670 system was used with two truncated constructs of E protein, the N-terminal transmembrane domain
671 (ET) (residues 1-39) and the C-terminal cytoplasmic domain (EC) (residues 36-75) (Fig 2B). Two EF
672 mutant proteins, N15A EF and V25F EF were generated using a site-directed mutagenesis kit
673 (www.neb.com).

674 **Protein expression and purification**

675 *E. coli* strain C43(DE3) (www.lucigen.com) cells transformed with the plasmid vectors carrying the
676 target E protein constructs were grown in minimal medium with 1 g/L ($^{15}\text{NH}_4$) $_2$ SO $_4$ as the sole nitrogen
677 source for producing uniformly ^{15}N -labeled samples [69] and with 2 g/L $^{13}\text{C}_6$ D-glucose as the carbon
678 source for uniformly $^{13}\text{C}/^{15}\text{N}$ - double-labeled proteins. For selectively (by residue type) ^{15}N -labeled
679 samples, the minimal medium with unlabeled ammonium sulfate was supplemented with 100–500 mg/L
680 of each of 19 amino acid residues and 100 mg/L of the ^{15}N -labeled amino acid. The isotopically labeled
681 compounds were obtained from Cambridge Isotope Laboratories (www.isotope.com). A preculture was
682 grown overnight in 50 mL of Luria-Bertani (LB) broth, then a 1% (v/v) aliquot of the preculture was
683 added to 500 mL of the minimal medium in a two-liter flask. The culture was maintained at 37°C with
684 shaking at 200 rpm until a cell density with an OD $_{600}$ of 0.5 was reached. Expression of the KSI-E
685 protein fusion proteins was induced by adding isopropyl β -D-1-thiogalactopyranoside (IPTG) to a final
686 concentration of 1 mM. After growth for 3 hr (Fig 2C lane 2) the cells were harvested by centrifugation
687 at 5,000 xg for 20 min at 4°C. The cell pellet was stored at -80°C overnight.

688 The cell pellet was resuspended in 72 mL of a solution containing 20 mM Tris-HCl, 500 mM NaCl,
689 pH 8 with 50 μ g/mL lysozyme, and 250 units Benzonase nuclease (www.sigmaaldrich.com) per liter of
690 culture. The cell lysate was sonicated (duty cycle 20%, output control 4, Sonic Dismembrator 550,
691 Fisher Scientific) for 10 minutes on ice. 8 mL of 20% (v/v) Triton X-100 was added to the cell lysate to a
692 final concentration of 2% (v/v) and incubated with gentle rotation for one hr at room temperature. The
693 cell lysate was then centrifuged at 20,000 xg for 30 min at 4°C. The supernatant was discarded, and
694 the pellet containing the inclusion bodies was resuspended in 40 mL of 20 mM HEPES, 500 mM NaCl,
695 pH 7.8. 400 mg of n-hexadecylphosphocholine (HPC, fos-choline 16, www.anatrace.com) was added to
696 the suspension at a 1% (w/v) final concentration and Tris (2-carboxyethyl) phosphine hydrochloride
697 (TCEP-HCl) at a final concentration of 1 mM; it was incubated with stirring for 2 hr at room temperature
698 or until the inclusion bodies were completely dissolved. The solubilized inclusion bodies were
699 centrifuged at 40,000 xg for 30 min at 15°C. The supernatant was loaded onto a Ni-NTA superflow
700 (www.qiagen.com) column equilibrated with HPC binding buffer (0.05% HPC, 20 mM HEPES, 500 mM
701 NaCl, pH 7.8) (Fig 2C lane 3). The column was washed with five-bed volumes of HPC binding buffer
702 and then 10-bed volumes of HPC washing buffer (0.05% HPC, 20 mM HEPES, 500 mM NaCl, 20 mM
703 imidazole, pH 7.8) (Fig 2C lane 4). The KSI-E protein fusion proteins were eluted with two-bed volumes
704 of HPC elution buffer (0.05% HPC, 20 mM HEPES, 500 mM NaCl, 500 mM imidazole, pH 7.8).

705 The fractions containing the fusion protein were pooled and dialyzed overnight against thrombin
706 cleavage buffer (20 mM HEPES, 50 mM NaCl, 1 mM EDTA, pH 7.8) in a 10 kDa MW cutoff dialysis
707 membrane (www.spectrumchemical.com). Approximately 50 mg of uniformly ¹⁵N labeled KSI-E protein
708 fusion protein was obtained from 1L of culture (Fig 2C lane 5). 10 units of high-purity thrombin
709 (www.mpbio.com) per mg of fusion protein were added to the dialyzed solution and incubated overnight
710 at room temperature with gentle rotation (Fig 2C lane 6). Importantly, thrombin retains its specificity and
711 protease activity in the presence of dilute HPC. The mixture of thrombin-cleaved polypeptides was
712 loaded onto a Ni affinity column equilibrated with HPC binding buffer and the flowthrough containing the

713 target E protein was pooled. Typically, a yield of 10 mg of highly pure ^{15}N -uniformly labeled E protein
714 was obtained from one liter of cell culture (Fig 2C lane 7). The TM domain of E (ET), the cytoplasmic
715 domain of E (EC), and the single-site mutants of EF, N15A and V25F, were all prepared following
716 essentially the same protocol and resulted in similar yields.

717 **Electrophoresis**

718 SDS-PAGE was performed using NuPAGE 4-12% Bis-Tris gels in 2-(N-morpholino)ethane sulfonic acid
719 (MES) buffer at room temperature. The protein bands were visualized by Coomassie blue staining (Fig
720 2C). PFO (perfluorooctanoic acid)-PAGE was performed as previously described [32, 70] using Novex
721 4-20% Tris-Glycine gels without SDS. The NuPAGE and Novex precast gels were obtained from
722 Invitrogen (www.thermofisher.com). 5 μg protein samples in HPC binding buffer were mixed with the
723 same volume of the PFO sample buffer (100 mM Tris base, 4% (w/v) NaPFO (www.alfa.com), 20%
724 (v/v) glycerol, 0.05% bromophenol blue, pH 8.0), vortex-mixed, centrifuged for five minutes at 12,000 $\times g$
725 and then applied to the gel. PFO-PAGE was performed with a precooled PFO running buffer (25 mM
726 Tris base, 192 mM glycine, 0.5% (w/v) PFO, pH 8.5) at 120 V for 3.5 hours in a cold room at 4°C. The
727 protein bands were visualized by Coomassie blue staining (Fig 8D).

728 **Sample preparation and NMR experiments**

729 Samples for solution NMR experiments were prepared by concentrating the purified proteins with
730 Amicon Ultra-4 10K centrifugal filters (www.endmillipore.com). Samples of 0.5 mM uniformly ^{15}N -
731 labeled and selectively ^{15}N -Leu and ^{15}N -Val labeled E protein in 5% (w/v) (123 mM) HPC, 20 mM
732 HEPES, 50 mM NaCl, 10% (v/v) $^2\text{H}_2\text{O}$, 1 mM DSS, pH 6.5 were used for the two-dimensional $^1\text{H}/^{15}\text{N}$
733 HSQC, $^1\text{H}/^{15}\text{N}$ HSQC-NOESY, $^1\text{H}/^{15}\text{N}$ heteronuclear NOE, and $^1\text{H}/^{15}\text{N}$ IPAP-HSQC experiments [71].
734 Samples of 1 mM uniformly $^{13}\text{C},^{15}\text{N}$ -double labeled proteins in 7% (w/v) (172 mM) HPC, 20 mM
735 HEPES, 50 mM NaCl, 10% (v/v) $^2\text{H}_2\text{O}$, 1 mM DSS, pH 6.5 were used for the three-dimensional HNCA,

736 HN(CO)CA, HNCO, and HN(CA)CO experiments [56]. TCEP-HCl was added to the EF and EC
737 samples at a final concentration of 10 mM.

738 ^{15}N - ^1H residual dipolar couplings (RDCs) were measured by comparison of the $^1J_{\text{NH}}$ couplings of
739 isotropic and weakly aligned EF samples. Weak alignment was induced and maintained by addition of
740 Y21M fd bacteriophage to the protein-containing micelle solutions at a final concentration of 20 mg/mL
741 [72].

742 The NMR experiments were performed on triple-resonance Bruker Avance 800 and Avance 600
743 spectrometers at 50°C. The two-dimensional $^1\text{H}/^{15}\text{N}$ HSQC-NOESY data were obtained using 100 ms
744 and 200 ms mix times. $^1\text{H}/^{15}\text{N}$ heteronuclear NOE data were obtained with a recycle delay of 4 sec. ^1H
745 chemical shifts were referenced to 0 ppm for DSS. The NMR data were processed and analyzed using
746 the computer programs Bruker Topspin 4 (www.bruker.com), NMRpipe/NMR Draw [73], and NMR View
747 [74].

748 **Drug binding**

749 100 mM stock solutions of amiloride, 5'-(N, N-dimethyl)-amiloride (DMA), 5-N-ethyl-N-isopropyl amiloride
750 (EIPA), and 5-(N, N-hexamethylene)-amiloride (HMA) (www.caymanchem.com) were prepared by dissolving
751 the appropriate amount of solid material in deuterated dimethyl sulfoxide (DMSO- d_6).

752 To observe the chemical shift perturbations of protein resonances by these compounds, two-
753 dimensional $^1\text{H}/^{15}\text{N}$ HSQC spectra were obtained from samples containing 0.2 mM uniformly ^{15}N -
754 labeled protein in the absence and presence of 2 mM amiloride, DMA, HMA, or EIPA. $^1\text{H}/^{15}\text{N}$ HSQC
755 spectra of uniformly ^{15}N -labeled EC in the absence and presence of 2 mM HMA were also obtained.
756 $^1\text{H}/^{15}\text{N}$ HSQC spectra of 0.2 mM uniformly ^{15}N -labeled ET with 0, 0.25, 0.5, 1, 1.5, and 2 mM HMA
757 present in the solution were obtained in order to track the chemical shift changes as a function of
758 concentration. All samples used in the binding experiments contained 2% (v/v) DMSO- d_6 at pH 6.5 to

759 ensure the absence of artifacts. The chemical shift perturbations were calculated using the equation
760 $CSP = [(\Delta\delta_H)^2 + (0.2\Delta\delta_N)^2]^{1/2}$, where $\Delta\delta_H$ is the change in the backbone amide 1H chemical shift and $\Delta\delta_N$
761 is the change in backbone amide ^{15}N chemical shift of an individual resolved and assigned resonance.

762 **SARS-CoV-2 antiviral test of amilorides**

763 Vero E6 and Caco-2 were obtained from ATCC and grown in DMEM (www.corning.com) with 10%
764 FBS, 10mM HEPES, and Penicillin-Streptomycin (www.thermofisher.com). SARS-CoV-2 isolate USA-
765 WA1/2020 (www.beiresources.org) was propagated on Caco-2 cells and infectious units quantified by
766 focus forming assay using Vero E6 (ATCC) cells. Approximately $10e4$ Vero E6 cells per well were
767 seeded in a 96-well plate and incubated overnight. Compounds or controls were added at the indicated
768 concentrations with addition of SARS-CoV-2 at a multiplicity of infection (MOI) equal to 1 or 0.1 as
769 indicated in Figs 7 and 8. After incubation for 18 hr for MOI 1 or 48 hr for MOI 0.1 at $37^\circ C$ and 5% CO_2 ,
770 the medium was removed, and the cells were incubated in 4% formaldehyde for 30 minutes at room
771 temperature. Formaldehyde fixed cells were washed with phosphate buffered saline and permeabilized
772 for immunofluorescence using 0.1% Triton X-100 in PBS with 1% bovine serum albumin (BSA) fraction
773 V (www.emdmillipore.com) and stained for SARS-CoV-2 with a primary anti-Nucleocapsid antibody
774 (www.genetex.com GTX135357) labeled with AlexaFluor 594. Cells were washed twice in PBS, and the
775 nuclei were stained with Sytox Green. Four to five images per well were obtained at 10x magnification
776 using an Incucyte S3 (Sartorius). The percent infected cells, nuclei count, and infected foci count were
777 calculated using built-in image analysis tools for the Incucyte S3. Foci were categorized as multi-cell
778 foci or single infected cell by repeating the analysis with area size restrictions in the red (nucleocapsid)
779 channel. IC_{50} and CC_{50} were determined using the nonlinear regression analysis in GraphPad Prism 9
780 with the bottom and top parameters constrained to 0 and 100, respectively. All work with authentic
781 SARS-CoV-2 was conducted under Biosafety Level-3 conditions at the University of California San
782 Diego. The reagent, SARS-Related Coronavirus 2, Isolate USA-WA1/2020, NR-52281 was deposited
783 by the Centers for Disease Control and Prevention and obtained through BEI Resources, NIAID, NIH.

784 **VLP assays**

785 For SARS-CoV-2 proteins, dsDNA gene fragments (gBlocks) encoding human-codon optimized
786 sequences for M, E, and N-V5, corresponding to those of the SARS-CoV-2 Wuhan-Hu-1 isolate
787 (genbank MN908947.3), were synthesized by Integrated DNA Technologies (www.idtdna.com). The
788 gene fragments were inserted into the pcDNA3.1(-) plasmid backbone between the NotI and EcoRI
789 restriction sites using In-Fusion Cloning (www.takarabio.com). The mutations in the transmembrane
790 region of the E protein were generated from the wild-type E protein construct using the QuikChange
791 site-directed mutagenesis kit (www.agilent.com) and verified by Sanger sequencing
792 (www.genewiz.com). HEK293T cells were cultured in complete Dulbecco's modified Eagle medium
793 containing 10% Fetal Bovine Serum and penicillin-streptomycin.

794 HEK293T cells were seeded in 6 well plates at a density of 250,000 cells/mL/well in complete
795 Dulbecco's modified Eagle medium (DMEM). The cells were transfected the following day with 500 ng
796 each of plasmids encoding the selected viral proteins and pcDNA2.3 plasmid backbone, using
797 Lipofectamine 2000 (www.thermofisher.com), according to the manufacturer's protocol (3,200 ng total
798 plasmid/well). Twenty-four hr after transfection, the supernatant from each well was clarified by
799 centrifugation at 1,000 xg for 5 min at 4°C. Clarified supernatants were then pelleted through 20%
800 sucrose for 1 hr at 23,500 xg and 4°C. Pelleted VLPs and cells were lysed in 1X TSDS-PAGE sample
801 buffer containing TCEP 1X Laemmli buffer with 50 mM Tris(2-carboxyethyl) phosphine
802 (www.sigmaaldrich.com) substituted for 2-mercaptoethanol. Cell lysates were boiled for 5 min prior to
803 use. Proteins in VLP and cell lysates were separated on 10% SDS-PAGE gels, transferred to PVDF
804 membranes, and immunoblotted with the following antibodies (Fig 7A): mouse monoclonal anti-V5 tag
805 (www.thermofisher.com, #R960-25), rabbit polyclonal anti-SARS M (generous gift of C. Machamer
806 [75]), rabbit polyclonal anti-SARS E (generous gift of C. Machamer [76]), and mouse monoclonal anti-
807 GAPDH (www.genetex.com, #GTX627408). Primary antibodies were detected using horseradish
808 peroxidase (HRP)-conjugated goat anti-mouse IgG (www.bio-rad.com) or HRP-donkey anti-rabbit IgG

809 (www.bio-rad.com) and Western Clarity detection reagent (www.bio-rad.com). Apparent molecular
810 masses were estimated using a commercial protein standard (www.thermofisher.com, PageRulePlus).
811 Chemiluminescence was detected using a Bio-Rad Chemi Doc imaging system and analyzed using
812 Bio-Rad Image Lab v5.1 software. Densitometry was performed using the Image Lab software
813 (www.bio-rad.com) and statistical significance was determined with Welch's *t*-test.

814 **Data deposition**

815 Backbone NMR resonances of full-length E protein was deposited in the BRMB (accession number:
816 50813).

817

818 **Acknowledgements**

819 We thank Francesca M. Marassi and Ye Tian for helpful discussions on the experimental results, and
820 Xuemei Huang and Jinghua Yu for assistance with the instrumentation.

821 **Author Contributions**

822 **Conceptualization:** Sang Ho Park, Aaron F. Carlin, John Guatelli, Stanley J. Opella.

823 **Data curation:** Sang Ho Park, Aaron L. Oom, John Guatelli, Stanley J. Opella.

824 **Formal analysis:** Sang Ho Park, Aaron L. Oom, Alex E. Clark, Aaron F. Carlin, John Guatelli, Stanley
825 J. Opella.

826 **Funding acquisition:** Ben A. Croker, Aaron F. Carlin, John Guatelli, Stanley J. Opella.

827 **Investigation:** Sang Ho Park, Haley Siddiqi, Daniela V. Castro, Aaron L. Oom, Anna De Angelis,
828 Charlotte A. Stoneham, Mary K. Lewinski, Alex E. Clark, Ben A. Croker, Aaron F. Carlin, John Guatelli,
829 Stanley J. Opella.

830 **Methodology:** Sang Ho Park, Aaron F. Carlin, John Guatelli, Stanley J. Opella.

831 **Project administration:** John Guatelli, Stanley J. Opella.

832 **Resources:** Alex E. Clark, Ben A. Croker, Aaron F. Carlin, John Guatelli, Stanley J. Opella.

833 **Supervision:** Sang Ho Park, John Guatelli, Stanley J. Opella.

834 **Validation:** Sang Ho Park, Aaron L. Oom, Aaron F. Carlin, John Guatelli, Stanley J. Opella.

835 **Visualization:** Sang Ho Park, Aaron L. Oom.

836 **Writing – original draft:** Sang Ho Park, Stanley J. Opella.

837 **Writing – review & editing:** Sang Ho Park, Anna De Angelis, Aaron L. Oom, Charlotte A. Stoneham,
838 Mary K. Lewinski, Alex E. Clark, Ben A. Croker, Aaron F. Carlin, John Guatelli, Stanley J. Opella.

839 References

- 840 1. Coronaviridae Study Group of the International Committee on Taxonomy of V. The
841 species Severe acute respiratory syndrome-related coronavirus: classifying 2019-nCoV and naming it
842 SARS-CoV-2. *Nat Microbiol.* 2020;5(4):536-44. Epub 2020/03/04. doi: 10.1038/s41564-020-0695-z.
843 PubMed PMID: 32123347; PubMed Central PMCID: PMC7095448.
- 844 2. Aronin SI, Sadigh M. Severe acute respiratory syndrome. *Conn Med.* 2004;68(4):207-15.
845 Epub 2004/04/21. PubMed PMID: 15095827.
- 846 3. de Groot RJ, Baker SC, Baric RS, Brown CS, Drosten C, Enjuanes L, et al. Middle East
847 respiratory syndrome coronavirus (MERS-CoV): announcement of the Coronavirus Study Group. *J*
848 *Viro.* 2013;87(14):7790-2. Epub 2013/05/17. doi: 10.1128/JVI.01244-13. PubMed PMID: 23678167;
849 PubMed Central PMCID: PMC3700179.
- 850 4. Wu F, Zhao S, Yu B, Chen YM, Wang W, Song ZG, et al. A new coronavirus associated
851 with human respiratory disease in China. *Nature.* 2020;579(7798):265-9. Epub 2020/02/06. doi:
852 10.1038/s41586-020-2008-3. PubMed PMID: 32015508; PubMed Central PMCID: PMC7094943.
- 853 5. Li YD, Chi WY, Su JH, Ferrall L, Hung CF, Wu TC. Coronavirus vaccine development:
854 from SARS and MERS to COVID-19. *J Biomed Sci.* 2020;27(1):104. Epub 2020/12/21. doi:
855 10.1186/s12929-020-00695-2. PubMed PMID: 33341119; PubMed Central PMCID: PMC7749790.
- 856 6. Heaton PM. The Covid-19 Vaccine-Development Multiverse. *N Engl J Med.*
857 2020;383(20):1986-8. Epub 2020/07/15. doi: 10.1056/NEJMe2025111. PubMed PMID: 32663910;
858 PubMed Central PMCID: PMC7377255.
- 859 7. Ogando NS, Dalebout TJ, Zevenhoven-Dobbe JC, Limpens R, van der Meer Y, Caly L, et
860 al. SARS-coronavirus-2 replication in Vero E6 cells: replication kinetics, rapid adaptation and
861 cytopathology. *J Gen Virol.* 2020;101(9):925-40. Epub 2020/06/23. doi: 10.1099/jgv.0.001453. PubMed
862 PMID: 32568027; PubMed Central PMCID: PMC7654748.
- 863 8. Neuman BW, Kiss G, Kunding AH, Bhella D, Baksh MF, Connelly S, et al. A structural
864 analysis of M protein in coronavirus assembly and morphology. *J Struct Biol.* 2011;174(1):11-22. Epub
865 2010/12/07. doi: 10.1016/j.jsb.2010.11.021. PubMed PMID: 21130884; PubMed Central PMCID:
866 PMC4486061.
- 867 9. Surya W, Li Y, Torres J. Structural model of the SARS coronavirus E channel in LMPG
868 micelles. *Biochim Biophys Acta Biomembr.* 2018;1860(6):1309-17. Epub 2018/02/24. doi:
869 10.1016/j.bbamem.2018.02.017. PubMed PMID: 29474890; PubMed Central PMCID:
870 PMC7094280.
- 871 10. Mandala VS, McKay MJ, Shcherbakov AA, Dregni AJ, Kolocouris A, Hong M. Structure
872 and drug binding of the SARS-CoV-2 envelope protein transmembrane domain in lipid bilayers. *Nat*
873 *Struct Mol Biol.* 2020;27(12):1202-8. Epub 2020/11/13. doi: 10.1038/s41594-020-00536-8. PubMed
874 PMID: 33177698; PubMed Central PMCID: PMC7718435.
- 875 11. Walls AC, Tortorici MA, Bosch BJ, Frenz B, Rottier PJM, DiMaio F, et al. Cryo-electron
876 microscopy structure of a coronavirus spike glycoprotein trimer. *Nature.* 2016;531(7592):114-7. Epub

- 877 2016/02/09. doi: 10.1038/nature16988. PubMed PMID: 26855426; PubMed Central PMCID:
878 PMCPMC5018210.
- 879 12. Schoeman D, Fielding BC. Coronavirus envelope protein: current knowledge. *Virology*.
880 2019;16(1):69. Epub 2019/05/28. doi: 10.1186/s12985-019-1182-0. PubMed PMID: 31133031; PubMed
881 Central PMCID: PMCPMC6537279.
- 882 13. DeDiego ML, Alvarez E, Almazan F, Rejas MT, Lamirande E, Roberts A, et al. A severe
883 acute respiratory syndrome coronavirus that lacks the E gene is attenuated in vitro and in vivo. *J Virol*.
884 2007;81(4):1701-13. Epub 2006/11/17. doi: 10.1128/JVI.01467-06. PubMed PMID: 17108030; PubMed
885 Central PMCID: PMCPMC1797558.
- 886 14. Kuo L, Hurst KR, Masters PS. Exceptional flexibility in the sequence requirements for
887 coronavirus small envelope protein function. *J Virol*. 2007;81(5):2249-62. Epub 2006/12/22. doi:
888 10.1128/JVI.01577-06. PubMed PMID: 17182690; PubMed Central PMCID: PMCPMC1865940.
- 889 15. Ortego J, Ceriani JE, Patino C, Plana J, Enjuanes L. Absence of E protein arrests
890 transmissible gastroenteritis coronavirus maturation in the secretory pathway. *Virology*.
891 2007;368(2):296-308. Epub 2007/08/19. doi: 10.1016/j.virol.2007.05.032. PubMed PMID: 17692883.
- 892 16. Opella SJ. Relating structure and function of viral membrane-spanning miniproteins. *Curr*
893 *Opin Virol*. 2015;12:121-5. Epub 2015/06/10. doi: 10.1016/j.coviro.2015.05.006. PubMed PMID:
894 26057606; PubMed Central PMCID: PMCPMC4476644.
- 895 17. Pervushin K, Tan E, Parthasarathy K, Lin X, Jiang FL, Yu D, et al. Structure and inhibition
896 of the SARS coronavirus envelope protein ion channel. *PLoS Pathog*. 2009;5(7):e1000511. Epub
897 2009/07/14. doi: 10.1371/journal.ppat.1000511. PubMed PMID: 19593379; PubMed Central PMCID:
898 PMCPMC2702000.
- 899 18. Li Y, Surya W, Claudine S, Torres J. Structure of a conserved Golgi complex-targeting
900 signal in coronavirus envelope proteins. *J Biol Chem*. 2014;289(18):12535-49. Epub 2014/03/29. doi:
901 10.1074/jbc.M114.560094
902 M114.560094 [pii]. PubMed PMID: 24668816; PubMed Central PMCID: PMC4007446.
- 903 19. Opella SJ, Marassi FM. Applications of NMR to membrane proteins. *Arch Biochem*
904 *Biophys*. 2017;628:92-101. Epub 2017/05/23. doi: 10.1016/j.abb.2017.05.011. PubMed PMID:
905 28529197; PubMed Central PMCID: PMCPMC5657258.
- 906 20. Cross TA, Opella SJ. Structural properties of fd coat protein in sodium dodecyl sulfate
907 micelles. *Biochem Biophys Res Commun*. 1980;92(2):478-84. Epub 1980/01/29. doi: 10.1016/0006-
908 291x(80)90358-7. PubMed PMID: 6986868.
- 909 21. Frey L, Lakomek NA, Riek R, Bibow S. Micelles, Bicelles, and Nanodiscs: Comparing the
910 Impact of Membrane Mimetics on Membrane Protein Backbone Dynamics. *Angew Chem Int Ed Engl*.
911 2017;56(1):380-3. Epub 2016/11/25. doi: 10.1002/anie.201608246. PubMed PMID: 27882643; PubMed
912 Central PMCID: PMCPMC6680326.
- 913 22. Chipot C, Dehez F, Schnell JR, Zitzmann N, Pebay-Peyroula E, Catoire LJ, et al.
914 Perturbations of Native Membrane Protein Structure in Alkyl Phosphocholine Detergents: A Critical
915 Assessment of NMR and Biophysical Studies. *Chem Rev*. 2018;118(7):3559-607. Epub 2018/03/01.

- 916 doi: 10.1021/acs.chemrev.7b00570. PubMed PMID: 29488756; PubMed Central PMCID:
917 PMCPMC5896743.
- 918 23. Opella SJ. NMR and membrane proteins. *Nat Struct Biol.* 1997;4 Suppl:845-8. Epub
919 1997/10/23. PubMed PMID: 9377156.
- 920 24. Lim KP, Xu HY, Liu DX. Physical interaction between the membrane (M) and envelope (E)
921 proteins of the coronavirus avian infectious bronchitis virus (IBV). *Adv Exp Med Biol.* 2001;494:595-
922 602. Epub 2002/01/05. doi: 10.1007/978-1-4615-1325-4_88. PubMed PMID: 11774531.
- 923 25. Corse E, Machamer CE. The cytoplasmic tails of infectious bronchitis virus E and M
924 proteins mediate their interaction. *Virology.* 2003;312(1):25-34. Epub 2003/08/02. doi: 10.1016/s0042-
925 6822(03)00175-2. PubMed PMID: 12890618.
- 926 26. Wu Q, Zhang Y, Lu H, Wang J, He X, Liu Y, et al. The E protein is a multifunctional
927 membrane protein of SARS-CoV. *Genomics Proteomics Bioinformatics.* 2003;1(2):131-44. Epub
928 2005/01/01. doi: 10.1016/s1672-0229(03)01017-9. PubMed PMID: 15626343; PubMed Central PMCID:
929 PMCPMC5172412.
- 930 27. Toto A, Ma S, Malagrino F, Visconti L, Pagano L, Stromgaard K, et al. Comparing the
931 binding properties of peptides mimicking the Envelope protein of SARS-CoV and SARS-CoV-2 to the
932 PDZ domain of the tight junction-associated PALS1 protein. *Protein Sci.* 2020;29(10):2038-42. Epub
933 2020/08/22. doi: 10.1002/pro.3936. PubMed PMID: 32822073; PubMed Central PMCID:
934 PMCPMC7461438.
- 935 28. Gordon DE, Jang GM, Bouhaddou M, Xu J, Obernier K, White KM, et al. A SARS-CoV-2
936 protein interaction map reveals targets for drug repurposing. *Nature.* 2020;583(7816):459-68. Epub
937 2020/05/01. doi: 10.1038/s41586-020-2286-9. PubMed PMID: 32353859; PubMed Central PMCID:
938 PMCPMC7431030.
- 939 29. Wilson L, McKinlay C, Gage P, Ewart G. SARS coronavirus E protein forms cation-
940 selective ion channels. *Virology.* 2004;330(1):322-31. Epub 2004/11/06. doi:
941 10.1016/j.virol.2004.09.033. PubMed PMID: 15527857; PubMed Central PMCID: PMCPMC7111769.
- 942 30. Wilson L, Gage P, Ewart G. Hexamethylene amiloride blocks E protein ion channels and
943 inhibits coronavirus replication. *Virology.* 2006;353(2):294-306. Epub 2006/07/04. doi:
944 10.1016/j.virol.2006.05.028. PubMed PMID: 16815524; PubMed Central PMCID: PMCPMC7111787.
- 945 31. Ma C, Marassi FM, Jones DH, Straus SK, Bour S, Strebel K, et al. Expression,
946 purification, and activities of full-length and truncated versions of the integral membrane protein Vpu
947 from HIV-1. *Protein Sci.* 2002;11(3):546-57. Epub 2002/02/16. doi: 10.1110/ps.37302. PubMed PMID:
948 11847278; PubMed Central PMCID: PMCPMC2373459.
- 949 32. Park SH, Mrse AA, Nevzorov AA, Mesleh MF, Oblatt-Montal M, Montal M, et al. Three-
950 dimensional structure of the channel-forming trans-membrane domain of virus protein "u" (Vpu) from
951 HIV-1. *J Mol Biol.* 2003;333(2):409-24. Epub 2003/10/08. doi: 10.1016/j.jmb.2003.08.048. PubMed
952 PMID: 14529626.
- 953 33. Howell SC, Mesleh MF, Opella SJ. NMR structure determination of a membrane protein
954 with two transmembrane helices in micelles: MerF of the bacterial mercury detoxification system.

- 955 Biochemistry. 2005;44(13):5196-206. Epub 2005/03/30. doi: 10.1021/bi048095v. PubMed PMID:
956 15794657.
- 957 34. Cook GA, Stefer S, Opella SJ. Expression and purification of the membrane protein p7
958 from hepatitis C virus. Biopolymers. 2011;96(1):32-40. Epub 2010/06/19. doi: 10.1002/bip.21453.
959 PubMed PMID: 20560141; PubMed Central PMCID: PMCPMC2954269.
- 960 35. Park SH, Casagrande F, Chu M, Maier K, Kiefer H, Opella SJ. Optimization of purification
961 and refolding of the human chemokine receptor CXCR1 improves the stability of proteoliposomes for
962 structure determination. Biochim Biophys Acta. 2012;1818(3):584-91. Epub 2011/10/26. doi:
963 10.1016/j.bbamem.2011.10.008. PubMed PMID: 22024025; PubMed Central PMCID:
964 PMCPMC3777732.
- 965 36. Amin A, Sarwar A, Saleem MA, Latif Z, Opella S. Expression and Purification of
966 Transmembrane Protein MerE from Mercury-Resistant *Bacillus cereus*. J Microbiol Biotechnol.
967 2019;29(2):274-82. Epub 2017/08/09. doi: 10.4014/jmb.1704.04062. PubMed PMID: 28783894.
- 968 37. Kuliopulos A, Nelson NP, Yamada M, Walsh CT, Furie B, Furie BC, et al. Localization of
969 the affinity peptide-substrate inactivator site on recombinant vitamin K-dependent carboxylase. J Biol
970 Chem. 1994;269(33):21364-70. Epub 1994/08/19. PubMed PMID: 8063763.
- 971 38. Schiksnis RA, Bogusky MJ, Tsang P, Opella SJ. Structure and dynamics of the Pf1
972 filamentous bacteriophage coat protein in micelles. Biochemistry. 1987;26(5):1373-81. Epub
973 1987/03/10. doi: 10.1021/bi00379a025. PubMed PMID: 3567175.
- 974 39. McDonnell PA, Shon K, Kim Y, Opella SJ. fd coat protein structure in membrane
975 environments. J Mol Biol. 1993;233(3):447-63. Epub 1993/10/05. doi: 10.1006/jmbi.1993.1523.
976 PubMed PMID: 8411155.
- 977 40. Lee S, Mesleh MF, Opella SJ. Structure and dynamics of a membrane protein in micelles
978 from three solution NMR experiments. J Biomol NMR. 2003;26(4):327-34. Epub 2003/06/20. doi:
979 10.1023/a:1024047805043. PubMed PMID: 12815259.
- 980 41. Berkamp S, Park SH, De Angelis AA, Marassi FM, Opella SJ. Structure of monomeric
981 Interleukin-8 and its interactions with the N-terminal Binding Site-I of CXCR1 by solution NMR
982 spectroscopy. J Biomol NMR. 2017;69(3):111-21. Epub 2017/11/17. doi: 10.1007/s10858-017-0128-3.
983 PubMed PMID: 29143165; PubMed Central PMCID: PMCPMC5869024.
- 984 42. Kallick DA, Tessmer MR, Watts CR, Li CY. The use of dodecylphosphocholine micelles in
985 solution NMR. J Magn Reson B. 1995;109(1):60-5. Epub 1995/10/01. doi: 10.1006/jmrb.1995.1146.
986 PubMed PMID: 8581309.
- 987 43. Jaremko L, Jaremko M, Giller K, Becker S, Zweckstetter M. Conformational Flexibility in
988 the Transmembrane Protein TSPO. Chemistry. 2015;21(46):16555-63. Epub 2015/09/24. doi:
989 10.1002/chem.201502314. PubMed PMID: 26394723; PubMed Central PMCID: PMCPMC5654506.
- 990 44. Parthasarathy K, Lu H, Surya W, Vararattanavech A, Pervushin K, Torres J. Expression
991 and purification of coronavirus envelope proteins using a modified beta-barrel construct. Protein Expr
992 Purif. 2012;85(1):133-41. Epub 2012/07/24. doi: 10.1016/j.pep.2012.07.005. PubMed PMID: 22819936;
993 PubMed Central PMCID: PMCPMC7129850.

- 994 45. Parthasarathy K, Ng L, Lin X, Liu DX, Pervushin K, Gong X, et al. Structural flexibility of
995 the pentameric SARS coronavirus envelope protein ion channel. *Biophys J.* 2008;95(6):L39-41. Epub
996 2008/07/29. doi: 10.1529/biophysj.108.133041. PubMed PMID: 18658207; PubMed Central PMCID:
997 PMCPMC2527252.
- 998 46. Veglia G, Zeri AC, Ma C, Opella SJ. Deuterium/hydrogen exchange factors measured by
999 solution nuclear magnetic resonance spectroscopy as indicators of the structure and topology of
000 membrane proteins. *Biophys J.* 2002;82(4):2176-83. Epub 2002/03/28. doi: 10.1016/s0006-
001 3495(02)75564-1. PubMed PMID: 11916873; PubMed Central PMCID: PMCPMC1302011.
- 002 47. Wishart DS, Sykes BD. The ¹³C chemical-shift index: a simple method for the
003 identification of protein secondary structure using ¹³C chemical-shift data. *J Biomol NMR.*
004 1994;4(2):171-80. Epub 1994/03/01. doi: 10.1007/BF00175245. PubMed PMID: 8019132.
- 005 48. Mesleh MF, Veglia G, DeSilva TM, Marassi FM, Opella SJ. Dipolar waves as NMR maps
006 of protein structure. *J Am Chem Soc.* 2002;124(16):4206-7. Epub 2002/04/19. doi: 10.1021/ja0178665.
007 PubMed PMID: 11960438; PubMed Central PMCID: PMCPMC3272071.
- 008 49. Mesleh MF, Lee S, Veglia G, Thiriot DS, Marassi FM, Opella SJ. Dipolar waves map the
009 structure and topology of helices in membrane proteins. *J Am Chem Soc.* 2003;125(29):8928-35. Epub
010 2003/07/17. doi: 10.1021/ja034211q. PubMed PMID: 12862490; PubMed Central PMCID:
011 PMCPMC3272074.
- 012 50. Cook GA, Opella SJ. Secondary structure, dynamics, and architecture of the p7
013 membrane protein from hepatitis C virus by NMR spectroscopy. *Biochim Biophys Acta.*
014 2011;1808(6):1448-53. Epub 2010/08/24. doi: 10.1016/j.bbamem.2010.08.010. PubMed PMID:
015 20727850; PubMed Central PMCID: PMCPMC3046219.
- 016 51. Mesleh MF, Opella SJ. Dipolar Waves as NMR maps of helices in proteins. *J Magn*
017 *Reson.* 2003;163(2):288-99. Epub 2003/08/14. doi: 10.1016/s1090-7807(03)00119-8. PubMed PMID:
018 12914844.
- 019 52. Westerbeck JW, Machamer CE. A Coronavirus E Protein Is Present in Two Distinct Pools
020 with Different Effects on Assembly and the Secretory Pathway. *J Virol.* 2015;89(18):9313-23. Epub
021 2015/07/03. doi: 10.1128/JVI.01237-15. PubMed PMID: 26136577; PubMed Central PMCID:
022 PMCPMC4542375.
- 023 53. Choma C, Gratkowski H, Lear JD, DeGrado WF. Asparagine-mediated self-association of
024 a model transmembrane helix. *Nat Struct Biol.* 2000;7(2):161-6. Epub 2000/02/03. doi: 10.1038/72440.
025 PubMed PMID: 10655620.
- 026 54. Torres J, Maheswari U, Parthasarathy K, Ng L, Liu DX, Gong X. Conductance and
027 amantadine binding of a pore formed by a lysine-flanked transmembrane domain of SARS coronavirus
028 envelope protein. *Protein Sci.* 2007;16(9):2065-71. Epub 2007/09/04. doi: 10.1110/ps.062730007.
029 PubMed PMID: 17766393; PubMed Central PMCID: PMCPMC2206980.
- 030 55. Verdia-Baguena C, Nieto-Torres JL, Alcaraz A, DeDiego ML, Torres J, Aguilera VM, et al.
031 Coronavirus E protein forms ion channels with functionally and structurally-involved membrane lipids.
032 *Virology.* 2012;432(2):485-94. Epub 2012/07/27. doi: 10.1016/j.virol.2012.07.005. PubMed PMID:
033 22832120; PubMed Central PMCID: PMCPMC3438407.

- 034 56. Grzesiek S, Dobeli H, Gentz R, Garotta G, Labhardt AM, Bax A. 1H, 13C, and 15N NMR
035 backbone assignments and secondary structure of human interferon-gamma. *Biochemistry*.
036 1992;31(35):8180-90. Epub 1992/09/08. doi: 10.1021/bi00150a009. PubMed PMID: 1525157.
- 037 57. Marassi FM, Ma C, Gratkowski H, Straus SK, Strebel K, Oblatt-Montal M, et al.
038 Correlation of the structural and functional domains in the membrane protein Vpu from HIV-1. *Proc Natl*
039 *Acad Sci U S A*. 1999;96(25):14336-41. Epub 1999/12/10. doi: 10.1073/pnas.96.25.14336. PubMed
040 PMID: 10588706; PubMed Central PMCID: PMCPMC24437.
- 041 58. Park SH, Opella SJ. Tilt angle of a trans-membrane helix is determined by hydrophobic
042 mismatch. *J Mol Biol*. 2005;350(2):310-8. Epub 2005/06/07. doi: 10.1016/j.jmb.2005.05.004. PubMed
043 PMID: 15936031.
- 044 59. Wang J, Denny J, Tian C, Kim S, Mo Y, Kovacs F, et al. Imaging membrane protein
045 helical wheels. *J Magn Reson*. 2000;144(1):162-7. Epub 2000/04/28. doi: 10.1006/jmre.2000.2037.
046 PubMed PMID: 10783287.
- 047 60. Marassi FM, Opella SJ. A solid-state NMR index of helical membrane protein structure
048 and topology. *J Magn Reson*. 2000;144(1):150-5. Epub 2000/04/28. doi: 10.1006/jmre.2000.2035.
049 PubMed PMID: 10783285; PubMed Central PMCID: PMCPMC3437921.
- 050 61. Nishimura K, Kim S, Zhang L, Cross TA. The closed state of a H⁺ channel helical bundle
051 combining precise orientational and distance restraints from solid state NMR. *Biochemistry*.
052 2002;41(44):13170-7. Epub 2002/10/31. doi: 10.1021/bi0262799. PubMed PMID: 12403618.
- 053 62. Takano T, Nakano K, Doki T, Hohdatsu T. Differential effects of viroporin inhibitors against
054 feline infectious peritonitis virus serotypes I and II. *Arch Virol*. 2015;160(5):1163-70. Epub 2015/02/24.
055 doi: 10.1007/s00705-015-2370-x. PubMed PMID: 25701212; PubMed Central PMCID:
056 PMCPMC7086594.
- 057 63. Ewart GD, Mills K, Cox GB, Gage PW. Amiloride derivatives block ion channel activity and
058 enhancement of virus-like particle budding caused by HIV-1 protein Vpu. *Eur Biophys J*. 2002;31(1):26-
059 35. Epub 2002/06/06. doi: 10.1007/s002490100177. PubMed PMID: 12046895.
- 060 64. Premkumar A, Wilson L, Ewart GD, Gage PW. Cation-selective ion channels formed by
061 p7 of hepatitis C virus are blocked by hexamethylene amiloride. *FEBS Lett*. 2004;557(1-3):99-103.
062 Epub 2004/01/27. doi: 10.1016/s0014-5793(03)01453-4. PubMed PMID: 14741348.
- 063 65. Cady SD, Schmidt-Rohr K, Wang J, Soto CS, Degrado WF, Hong M. Structure of the
064 amantadine binding site of influenza M2 proton channels in lipid bilayers. *Nature*. 2010;463(7281):689-
065 92. Epub 2010/02/05. doi: 10.1038/nature08722. PubMed PMID: 20130653; PubMed Central PMCID:
066 PMCPMC2818718.
- 067 66. David P, Mayan H, Cragoe EJ, Jr., Karlsh SJ. Structure-activity relations of amiloride
068 derivatives, acting as antagonists of cation binding on Na⁺/K⁺-ATPase. *Biochim Biophys Acta*.
069 1993;1146(1):59-64. Epub 1993/02/23. doi: 10.1016/0005-2736(93)90338-z. PubMed PMID: 8382955.
- 070 67. Westerbeck JW, Machamer CE. The Infectious Bronchitis Coronavirus Envelope Protein
071 Alters Golgi pH To Protect the Spike Protein and Promote the Release of Infectious Virus. *J Virol*.
072 2019;93(11). Epub 2019/03/15. doi: 10.1128/JVI.00015-19. PubMed PMID: 30867314; PubMed Central
073 PMCID: PMCPMC6532078.

- 074 68. Gratkowski H, Lear JD, DeGrado WF. Polar side chains drive the association of model
075 transmembrane peptides. *Proc Natl Acad Sci U S A*. 2001;98(3):880-5. Epub 2001/02/07. doi:
076 10.1073/pnas.98.3.880. PubMed PMID: 11158564; PubMed Central PMCID: PMCPMC14678.
- 077 69. Cross TA, DiVerdi JA, Opella SJ. Strategy for nitrogen NMR analysis of biopolymers.
078 *Journal of the American Chemical Society*. 1982;104(6):1759-61. doi: 10.1021/ja00370a062.
- 079 70. Ramjeesingh M, Huan LJ, Garami E, Bear CE. Novel method for evaluation of the
080 oligomeric structure of membrane proteins. *Biochem J*. 1999;342 (Pt 1):119-23. Epub 1999/08/05.
081 PubMed PMID: 10432308; PubMed Central PMCID: PMCPMC1220444.
- 082 71. Ottiger M, Delaglio F, Bax A. Measurement of J and dipolar couplings from simplified two-
083 dimensional NMR spectra. *J Magn Reson*. 1998;131(2):373-8. Epub 1998/05/08. doi:
084 10.1006/jmre.1998.1361. PubMed PMID: 9571116.
- 085 72. Park SH, Son WS, Mukhopadhyay R, Valafar H, Opella SJ. Phage-induced alignment of
086 membrane proteins enables the measurement and structural analysis of residual dipolar couplings with
087 dipolar waves and lambda-maps. *J Am Chem Soc*. 2009;131(40):14140-1. Epub 2009/09/19. doi:
088 10.1021/ja905640d. PubMed PMID: 19761238; PubMed Central PMCID: PMC2771775.
- 089 73. Delaglio F, Grzesiek S, Vuister GW, Zhu G, Pfeifer J, Bax A. NMRPipe: a
090 multidimensional spectral processing system based on UNIX pipes. *J Biomol NMR*. 1995;6(3):277-93.
091 Epub 1995/11/01. doi: 10.1007/BF00197809. PubMed PMID: 8520220.
- 092 74. Johnson BA, Blevins RA. NMR View: A computer program for the visualization and
093 analysis of NMR data. *J Biomol NMR*. 1994;4(5):603-14. Epub 1994/09/01. doi: 10.1007/BF00404272.
094 PubMed PMID: 22911360.
- 095 75. McBride CE, Li J, Machamer CE. The cytoplasmic tail of the severe acute respiratory
096 syndrome coronavirus spike protein contains a novel endoplasmic reticulum retrieval signal that binds
097 COPI and promotes interaction with membrane protein. *J Virol*. 2007;81(5):2418-28. Epub 2006/12/15.
098 doi: 10.1128/JVI.02146-06. PubMed PMID: 17166901; PubMed Central PMCID: PMCPMC1865919.
- 099 76. Cohen JR, Lin LD, Machamer CE. Identification of a Golgi complex-targeting signal in the
100 cytoplasmic tail of the severe acute respiratory syndrome coronavirus envelope protein. *J Virol*.
101 2011;85(12):5794-803. Epub 2011/04/01. doi: 10.1128/JVI.00060-11. PubMed PMID: 21450821;
102 PubMed Central PMCID: PMCPMC3126292.
- 103 77. Park SH, De Angelis AA, Nevzorov AA, Wu CH, Opella SJ. Three-dimensional structure of
104 the transmembrane domain of Vpu from HIV-1 in aligned phospholipid bicelles. *Biophys J*.
105 2006;91(8):3032-42. Epub 2006/07/25. doi: 10.1529/biophysj.106.087106. PubMed PMID: 16861273;
106 PubMed Central PMCID: PMCPMC1578490.
- 107 78. Grant CV, Yang Y, Glibowicka M, Wu CH, Park SH, Deber CM, et al. A Modified
108 Alderman-Grant Coil makes possible an efficient cross-coil probe for high field solid-state NMR of lossy
109 biological samples. *J Magn Reson*. 2009;201(1):87-92. Epub 2009/09/08. doi:
110 10.1016/j.jmr.2009.08.009. PubMed PMID: 19733108; PubMed Central PMCID: PMCPMC2800166.
111

112 Supporting information captions

113 **S1 Fig. Sequence alignment of coronavirus E proteins.** Three subgroups are indicated. The numbers at the
114 top of the amino acid sequence corresponds to SARS-CoV-2 E protein.

115 **S2 Fig. DNA sequence of intact full-length E protein with codons optimized for expression in *E. coli*.** The
116 N-terminal linker sequence containing a ten histidine tag and a thrombin cleavage site is shown in italics. The
117 sequences in bold contain the multiple restriction sites for cloning. AlwNI and XhoI sites were inserted for KSI-
118 fusion system with pET31b(+) vector (www.emdmillipore.com). BamHI and SacI sites were inserted for GST-
119 fusion system using pGEX-2T vector (www.sigmaaldrich.com).

120 **S3 Fig. $^1\text{H}/^{15}\text{N}$ HSQC NMR spectrum of 0.5 mM uniformly ^{15}N -labeled full-length E protein (residues 1-75) in**
121 **100 mM HPC at 50°C.** The spectrum was obtained at a ^1H resonance frequency of 800 MHz Resonance
122 assignments are marked.

123 **S4 Fig. Comparison of $^1\text{H}/^{15}\text{N}$ HSQC NMR spectra of uniformly ^{15}N -labeled full-length E protein (EF)**
124 **(residues 1-75) with two selectively ^{15}N labeled E proteins.** A. ^{15}N -Leu labeled EF. B. ^{15}N -Val labeled EF. The
125 spectra of selectively labeled EF (red contours) are superimposed on that of uniformly labeled EF (black
126 contours). Resonance assignments of the selectively labeled spectra are marked. The positions of the leucine
127 and valine residues are indicated in red in the sequence of E protein.

128 **S5 Fig. Comparison of $^1\text{H}/^{15}\text{N}$ HSQC NMR spectra of uniformly ^{15}N -labeled full-length E protein (EF)**
129 **(residues 1-75) with two truncated constructs.** A. E protein transmembrane domain (ET) (residues 1-39). B. E
130 protein cytoplasmic domain (EC) (residues 36-75). The spectra of the truncated constructs (red contours) are
131 superimposed on that of the full-length E protein (EF) (black contours). C. Chemical shift perturbation plot of ET
132 resonance frequencies compared to those of EF as a function of residue number.

133 **S6 Fig. Expanded region of $^1\text{H}/^{15}\text{N}$ IPAP spectra of full-length E protein (EF) (residues 1-75) in HPC**
134 **micelles.** A. Isotropic sample. B. Weakly aligned sample in the presence of Y21M fd bacteriophage at 20 mg/mL.
135 Residue numbers and $^1J_{\text{NH}}$ couplings are indicated in parenthesis, respectively.

136 **S7 Fig. One-dimensional oriented sample ^{15}N chemical shift solid-state NMR spectra.** A. Transmembrane
137 domain of E protein (ET) from SARS-CoV-2. B. Transmembrane domain of Virus Protein U (VPU) from HIV-1
138 [77]. The spectrum of ET sample was obtained at 35°C on a Bruker 900 MHz spectrometer using a home-built
139 $^1\text{H}/^{15}\text{N}$ double-resonance probe with a MAGC coli for the ^1H channel and a solenoid coil for the ^{15}N channel [78].
140 Uniformly ^{15}N -labeled ET was embedded in 1,2-dimyristoyl-sn-glycero-phosphocholine (DMPC) bilayers oriented
141 with the lipid bilayer normal perpendicular to the applied magnetic field. The molar ratio of DMPC to ET is 395:1
142 and the DMPC concentration is 30% (w/v). Fast uniaxial rotational diffusion of both proteins about the bilayer
143 normal yielded motionally averaged single line resonances. The spectra in blue are ^{15}N chemical shift projections

144 of the two-dimensional calculated PISA wheel spectra [59, 60] with (A) a 36-residue ideal helix ($\text{PHI}=-61^\circ$ and
145 $\text{PSI}=-45^\circ$) with its helix axis tilted 45° from the lipid bilayer normal and (B) a 18-residue ideal helix ($\text{PHI}=-61^\circ$ and
146 $\text{PSI}=-45^\circ$) with its helix axis tilted 30° from the lipid bilayer normal.

147

148 **S1 Table. Backbone resonance assignment and NH RDCs of full-length E protein in HPC micelles.**

149

150 **Supporting information**

151

152 **Interactions of SARS-CoV-2 envelope protein with amilorides correlate with**
153 **antiviral activity**

154 Sang Ho Park¹, Haley Siddiqi¹, Daniela V. Castro¹, Anna De Angelis¹, Aaron L. Oom², Charlotte A.
155 Stoneham³, Mary K. Lewinski³, Alex E. Clark^{3,4}, Ben A. Croker⁵, Aaron F. Carlin³, John Guatelli³, and
156 Stanley J. Opella^{1*}

157 ¹Department of Chemistry and Biochemistry, University of California San Diego, La Jolla, CA 92093, USA

158 ²Department of Medicine, University of California San Diego, La Jolla, CA 92093, USA.

159 ³Division of Infectious Diseases and Global Public Health, Department of Medicine; University of
160 California San Diego School of Medicine, 9500 Gilman Drive, La Jolla, CA 92093, USA.

161 ⁴Department of Cellular and Molecular Medicine, University of California San Diego, La Jolla, CA 92093,
162 USA.

163 ⁵Department of Pediatrics, University of California San Diego, La Jolla, CA, USA

164

165 Short title: Interactions of SARS-CoV-2 E with amilorides correlate with antiviral activity

166

167 *Corresponding author E-mail address: sopella@ucsd.edu

168

169

170

171

```

      5     10    15    20    25    30    35    40    45    50    55    60    65    70    75
SARS-CoV-2 MY--S---FVSEETGLIVNSVLLFLAFVVFLLVTLAILTALRLCAYCCNIVNVSLVKPTV----YVYSRV--KNLN SSR-----VPDLL-V
SARS-CoV   MY--S---FVSEETGLIVNSVLLFLAFVVFLLVTLAILTALRLCAYCCNIVNVSLVKPTV----YVYSRV--KNLN SSE-----VPDLL-V
β MERS-CoV  ML--P---FVQERIGLFIVNFFIFTVVCAITLLVCM AFLTATRLCVQCMTGFNTLLVQPAL----YLYNTQ--RSVYVKFGD-SKPPLPDEW-V
HCoV-OC43  MFMAD--AYLADTV-WYVGQII FIVAI C L L V T I V V V A F L A T F K L C I Q L C G M C N T L V L S P S I ----YVFNR--GRQFYEFYND- IKPPVLDVDD-V
HCoV-HKU1  --MVD--LFFNDTA-WYIGQILVLVLFCLISLIFVVAFLATIKLCMQLCGFCNFFIISP SA----YVYKR--GMQLYKSYSEQVIPPTSD-YL-I
MHV-A59    --MFN--LFLTDTV-WYVGQII FIFAVCLMVTII VVAFLASIKLCIQLCGLCNTLVLSPSI----YLYDR--SKQLYKYNEEMRLPLEVDD-I
α HCoV-229E MF--L---KLVDHA-LVNVLLWCVLI VILLVCITII KLIKLCFTCHMFCNRTVYGPIK----NVYHIY--QSYM-HI----DPFPRVID-F
HCoV-NL63  MF--L---RLIDDNG-IVNLSILWLVMIFFVFLAMTFIKLIQLCFTCHYFFSRTLYQPVY----KIFLAY--QDYM-QI----APVPAEVLN-V
γ IBV-Beaudette --MTNLLNKSLDEN-GSFLTALYIFVGFLALYLLGRALQAFVQAADACCLFWYTWVVVPGAKGTAFVYNHTYGGKLNKPELETVINEFFPKNGWKQ

```

172 **S1 Fig. Sequence alignment of coronavirus E proteins.** Three subgroups are indicated. The numbers at the
173 top of the amino acid sequence corresponds to SARS-CoV-2 E protein.

174

175

```

176 CAGATGCTGGATCCG GGG GGC AAG AAG CAT CAT CAC CAC CAC CAT CAC CAT CAC CAC
177 GGG GGC AAA AAA CTG GTT CCT CGT GGC TCC ATG TAT TCC TTT GTT TCT GAA GAG
178 ACC GGT ACG CTG ATT GTG AAC TCG GTA TTA CTG TTC TTA GCC TTC GTA GTT TTC
179 CTT TTA GTC ACG CTT GCG ATC CTT ACA GCT CTG CGC CTG TGT GCG TAT TGT TGT
180 AAC ATC GTA AAC GTA TCC TTG GTG AAG CCT ACT GTC TAT GTG TAC TCT CGT GTA
181 AAA AAT TTG AAC TCG TCA CGC GTT CCC GAT CTG TTA GTC TGA CTCGAGCTC

```

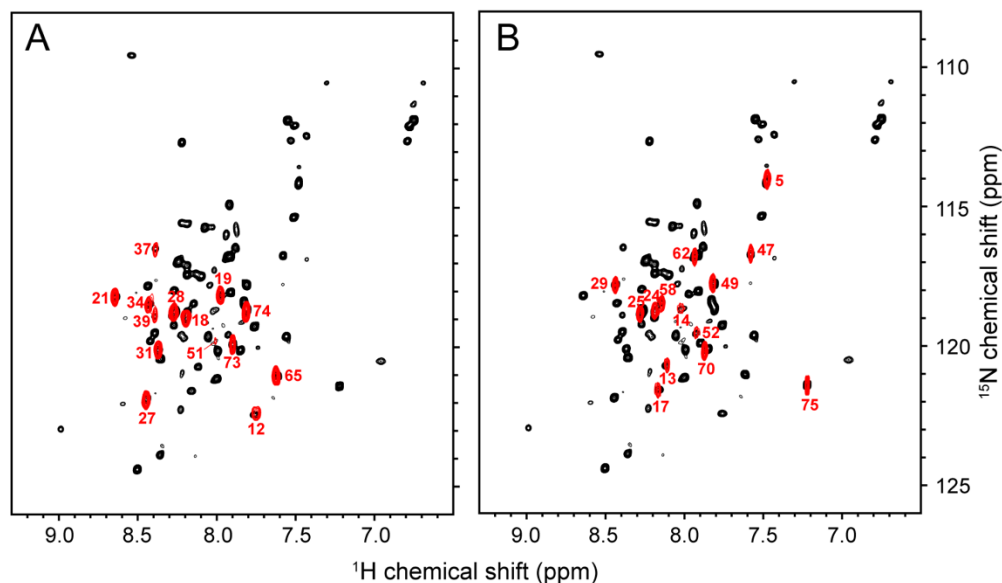
182 **S2 Fig. DNA sequence of intact full-length E protein with codons optimized for expression in *E. coli*.** The
183 N-terminal linker sequence containing a ten histidine tag and a thrombin cleavage site is shown in italics. The
184 sequences in bold contain the multiple restriction sites for cloning. AlwNI and XhoI sites were inserted for KSI-
185 fusion system with pET31b(+) vector (www.emdmillipore.com). BamHI and SacI sites were inserted for GST-
186 fusion system using pGEX-2T vector (www.sigmaaldrich.com).

187

195

196

MYSFVSEETGLIIVNSVLLFLAFVVFLLVTLAILTALRLCAYCCNIIVNSLVKPTVYVYSRVKLNSSRVPDLLV



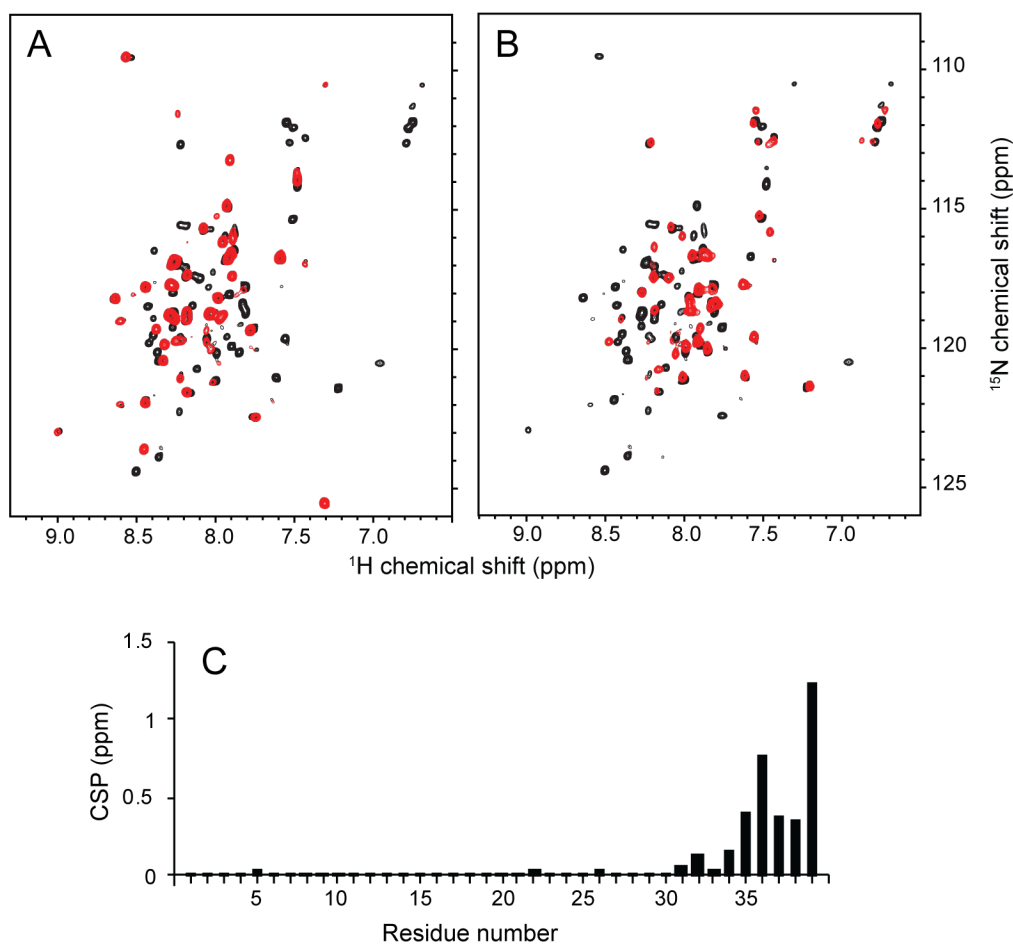
197

198 **S4 Fig. Comparison of $^1\text{H}/^{15}\text{N}$ HSQC NMR spectra of uniformly ^{15}N -labeled full-length E protein (EF)**
199 **(residues 1-75) with two selectively ^{15}N labeled E proteins. (A) ^{15}N -Leu labeled EF. (B) ^{15}N -Val labeled EF.**
200 The spectra of selectively labeled EF (red contours) are superimposed on that of uniformly labeled EF (black
201 contours). Resonance assignments of the selectively labeled spectra are marked. The positions of the leucine
202 and valine residues are indicated in red in the sequence of E protein.

203

204

205



206

207 **S5 Fig. Comparison of $^1\text{H}/^{15}\text{N}$ HSQC NMR spectra of uniformly ^{15}N -labeled full-length E protein (EF)**
208 **(residues 1-75) with two truncated constructs. (A) E protein transmembrane domain (ET) (residues 1-39). (B)**
209 **E protein cytoplasmic domain (EC) (residues 36-75). The spectra of the truncated constructs (red contours) are**
210 **superimposed on that of the full-length E protein (EF) (black contours). (C) Chemical shift perturbation plot of ET**
211 **resonance frequencies compared to those of EF as a function of residue number.**

212

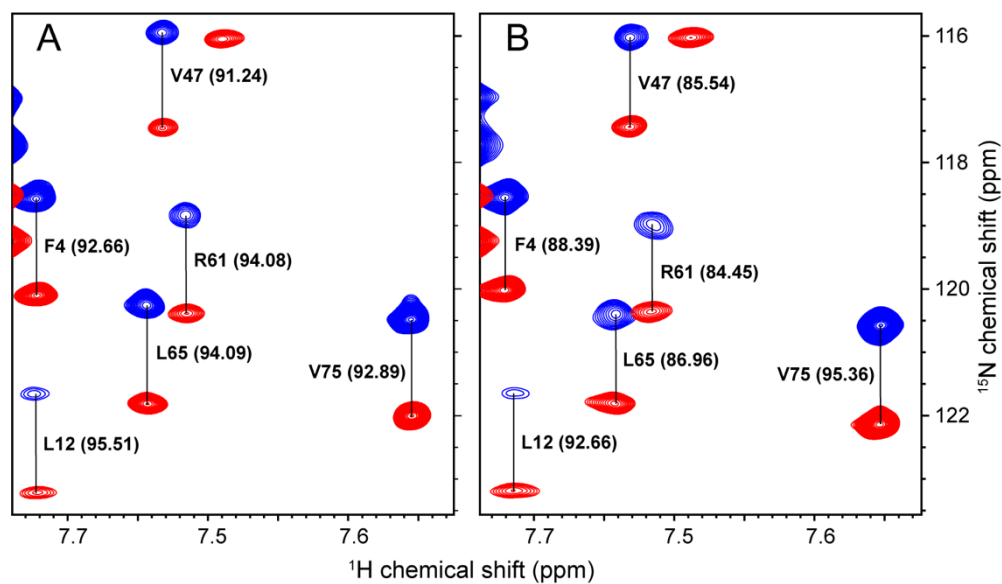
213

214

215

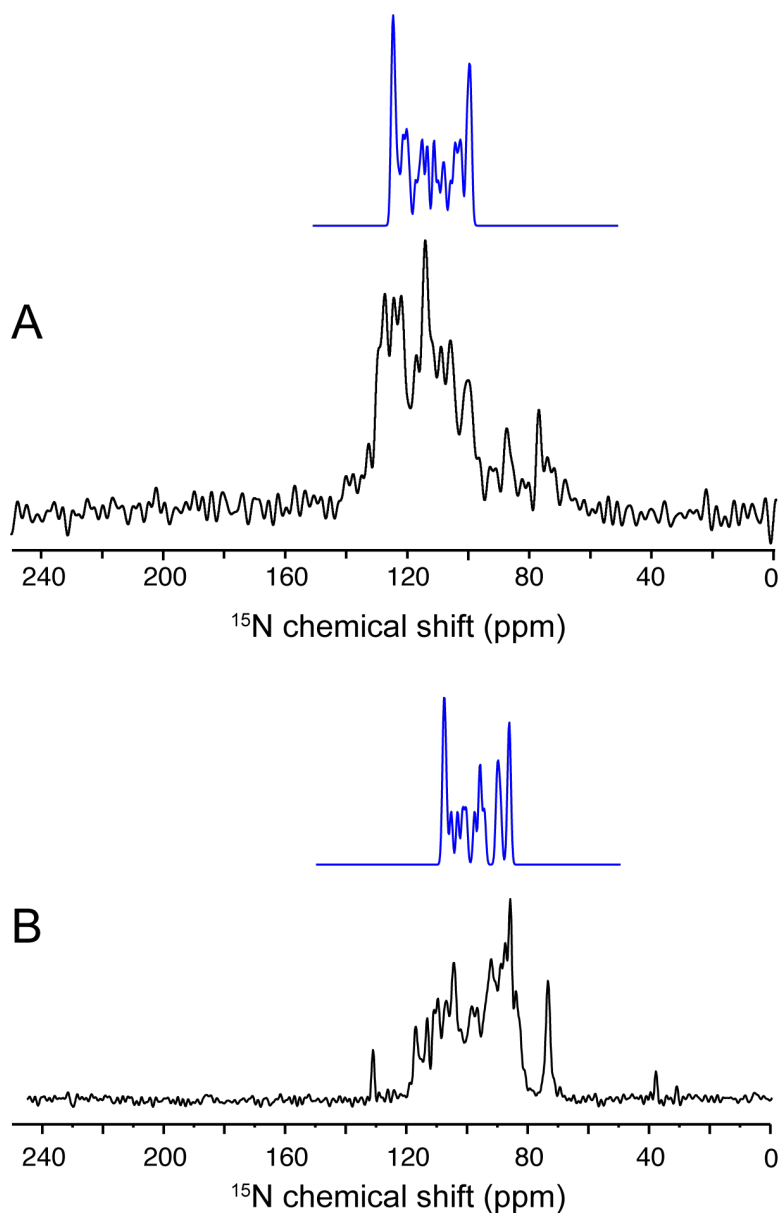
216

217



218

219 **S6 Fig. Expanded region of $^1\text{H}/^{15}\text{N}$ IPAP spectra of full-length E protein (EF) (residues 1-75) in HPC**
220 **micelles. (A) Isotropic sample. (B) Weakly aligned sample in the presence of Y21M fd bacteriophage at 20**
221 **mg/mL. Residue numbers and $^1J_{\text{NH}}$ couplings are indicated in parenthesis, respectively.**



222
223

224 **S7 Fig. One-dimensional oriented sample ^{15}N chemical shift solid-state NMR spectra.** (A) Transmembrane
225 domain of E protein (ET) from SARS-CoV-2. (B) Transmembrane domain of Virus Protein U (VPU) from HIV-1
226 [77]. The spectrum of the ET sample was obtained at 35°C on a Bruker 900 MHz spectrometer using a home-built
227 $^1\text{H}/^{15}\text{N}$ double-resonance probe with a MAGC coil for the ^1H channel and a solenoid coil for the ^{15}N channel [78].
228 Uniformly ^{15}N -labeled ET was embedded in 1,2-dimyristoyl-sn-glycero-phosphocholine (DMPC) bilayers oriented
229 with the lipid bilayer normal perpendicular to the applied magnetic field. The molar ratio of DMPC to ET was 395:1
230 and the DMPC concentration was 30% (w/v). Fast uniaxial rotational diffusion of both proteins about the bilayer
231 normal yielded motionally averaged single line resonances. The spectra in blue are ^{15}N chemical shift projections
232 of the two-dimensional calculated PISA wheel spectra [59, 60] with (A) a 36-residue ideal helix ($\text{PHI}=-61^\circ$ and
233 $\text{PSI}=-45^\circ$) with its helix axis tilted 45° from the lipid bilayer normal and (B) a 18-residue ideal helix ($\text{PHI}=-61^\circ$ and
234 $\text{PSI}=-45^\circ$) with its helix axis tilted 30° from the lipid bilayer normal.

235 **S1 Table. Backbone resonance assignment and NH RDCs of full-length E protein in HPC micelles.**

Resid	number	NH	15N	CA shift	CO shift	NH RDC
M	1	8.990	122.931	57.773	176.089	-2.86
Y	2	7.919	116.747	58.893	176.390	
S	3	7.921	114.872	60.298	174.761	1.43
F	4	7.760	119.246	59.365	175.286	-4.28
V	5	7.481	114.106	62.140	175.198	1.42
S	6	8.242	116.926	58.808	175.103	
E	7	8.598	122.019	58.719	178.061	-1.42
E	8	8.577	118.929	58.580	176.853	-1.34
T	9	7.876	115.829	65.811	175.949	6.25
G	10	8.540	109.520	47.297	174.952	7.66
T	11	7.939	115.917	65.742	175.523	0.01
L	12	7.762	122.407	58.262	179.461	-2.85
I	13	8.225	119.551	65.514	176.963	5.47
V	14	8.017	118.650	67.265	177.078	2.84
N	15	8.242	116.926	56.111	177.326	
S	16	8.077	115.681	63.352	175.469	2.07
V	17	8.160	121.552	67.144	177.586	9.48
L	18	8.190	118.966	58.621	178.348	0.55
L	19	7.970	118.093	58.285	177.894	-1.45
F	20	8.268	118.695	61.855	176.951	
L	21	8.643	118.184	58.035	178.178	5.70
A	22	8.360	120.410	55.612	178.456	1.43
F	23	8.187	117.385	61.528	176.581	2.31
V	24	8.189	118.727	67.483	177.894	4.86
V	25	8.268	118.695	67.829	177.045	
F	26	8.395	119.490	61.733	178.105	-2.85
L	27	8.446	121.848	58.304	177.894	1.77
L	28	8.268	118.695	58.415	178.617	
V	29	8.438	117.791	67.201	178.436	2.85
T	30	7.881	116.432	68.663	176.412	
L	31	8.370	120.095	58.144	179.838	5.70
A	32	8.505	124.376	55.910	178.692	4.28
I	33	8.272	117.959	65.871	177.718	-0.01
L	34	8.432	118.455	58.573	178.851	4.28
T	35	8.186	115.567	68.218	176.246	9.97
A	36	8.361	123.858	55.799	179.377	5.70
L	37	8.389	116.444	57.949	178.649	1.42

Resid	number	NH	15N	CA shift	CO shift	NH RDC
R	38	8.047	117.764	57.985	178.919	8.52
L	39	8.394	118.863	57.077		8.56
C	40			61.977	175.327	
A	41	8.230	122.237	54.581	178.267	-1.82
Y	42	7.884	116.422	59.824	176.854	7.33
C	43	8.031	115.681	60.727	174.876	2.99
C	44	8.019	117.248	60.158		-5.29
N	45	8.300	118.418	54.323	175.567	
I	46	7.828	118.354	62.515	175.562	
V	47	7.581	116.702	62.700	175.174	-5.70
N	48	8.056	119.603	53.545	175.154	-8.56
V	49	7.810	117.742	62.629	175.254	1.42
S	50	8.135	117.375	58.845		-0.06
L	51	8.012	119.860	55.800	177.905	
V	52	7.927	119.544	66.117	176.475	
K	53	8.272	119.204	60.393		-6.76
P	54			65.890	177.282	
T	55	7.432	112.404	67.457	176.185	-8.55
V	56	8.117	120.700	66.620	178.318	-11.40
Y	57	8.000	121.121	61.674	178.017	-4.28
V	58	8.146	118.426	67.393	177.426	-1.36
Y	59	8.422	119.762	61.661	176.551	-12.83
S	60	8.220	112.631	61.706	175.756	-8.55
R	61	7.558	119.592	57.242	177.417	-9.63
V	62	8.019	117.248	64.973	177.119	
K	63	7.828	118.354	58.385	176.704	
N	64	7.515	115.330	53.511	175.608	-9.99
L	65	7.616	121.004	56.176	176.465	-7.13
N	66	8.096	117.428	53.369	175.375	-5.35
S	67	8.224	115.539	59.418	174.884	0.00
S	68	8.189	117.062	59.493	174.269	5.78
R	69	7.994	120.114	55.850	175.984	-5.70
V	70	7.850	120.081	62.872		0.01
P	71			64.130	176.190	
D	72	7.914	118.016	55.115	176.190	2.85
L	73	7.898	119.889	55.726	176.420	-2.85
L	74	7.809	118.626	55.168	175.580	
V	75	7.222	121.375	63.256		2.47

237 References

- 238 1. Park SH, De Angelis AA, Nevzorov AA, Wu CH, Opella SJ. Three-dimensional structure of the
239 transmembrane domain of Vpu from HIV-1 in aligned phospholipid bicelles. *Biophys J*. 2006;91(8):3032-42. Epub
240 2006/07/25. doi: 10.1529/biophysj.106.087106. PubMed PMID: 16861273; PubMed Central PMCID:
241 PMC1578490.
- 242 2. Grant CV, Yang Y, Glibowicka M, Wu CH, Park SH, Deber CM, et al. A Modified Alderman-Grant Coil makes
243 possible an efficient cross-coil probe for high field solid-state NMR of lossy biological samples. *J Magn Reson*.
244 2009;201(1):87-92. Epub 2009/09/08. doi: 10.1016/j.jmr.2009.08.009. PubMed PMID: 19733108; PubMed Central
245 PMCID: PMC2800166.
- 246 3. Wang J, Denny J, Tian C, Kim S, Mo Y, Kovacs F, et al. Imaging membrane protein helical wheels. *J Magn*
247 *Reson*. 2000;144(1):162-7. Epub 2000/04/28. doi: 10.1006/jmre.2000.2037. PubMed PMID: 10783287.
- 248 4. Marassi FM, Opella SJ. A solid-state NMR index of helical membrane protein structure and topology. *J Magn*
249 *Reson*. 2000;144(1):150-5. Epub 2000/04/28. doi: 10.1006/jmre.2000.2035. PubMed PMID: 10783285; PubMed
250 Central PMCID: PMC3437921.

251

252

253